Scientific Reports

https://doi.org/10.1038/s41598-026-56733-w

Article in Press

Nonlinear vibration analysis of graphene nanoplatelet-reinforced polymer plates incorporating hyperelastic material behavior

Received: 1 April 2026

Accepted: 2 June 2026

Published online: 08 June 2026

Cite this article as: Saraghayn A.M., Ajri M., Alijani A. *et al.* Nonlinear vibration analysis of graphene nanoplatelet-reinforced polymer plates incorporating hyperelastic material behavior. *Sci Rep* (2026). https://doi.org/10.1038/s41598-026-56733-w

Abolfazl Mousazadeh Saraghayn, Masoud Ajri, Ali Alijani, Mohammad Salehpour & Vahid Arab Maleki

Nonlinear Vibration Analysis of Graphene Nanoplatelet-Reinforced Polymer Plates Incorporating Hyperelastic Material Behavior

Abolfazl Mousazadeh Saraghayn[a], Masoud Ajri[b,z,2], Ali Alijani[a], Mohammad Salehpour[a], Vahid Arab Maleki[c]

[a]Department of Mechanical Engineering, Islamic Azad University, Bandar Anzali, Iran

[b]Department of Mechanical Engineering, University of Mohaghegh Ardabili, Ardabil, 56199-13131, Iran

[c]Department of Mechanical Engineering, University of Maragheh, Maragheh, Iran

[z,2] Corresponding author
E-mail addresses: m.ajri@uma.ac.ir

Abstract

This research presents an analytical investigation into the nonlinear vibrational behavior of graphene nanoplatelet-reinforced polymer (GPL-R) plates subjected to external excitation. The novelty of the proposed methodology lies in establishing a direct test-to-dynamics framework in which tensile-test-derived Mooney–Rivlin constants are embedded into the forced nonlinear vibration formulation of GPL-reinforced polymer plates, rather than treating the nanocomposite as an equivalent linear elastic or purely homogenized material. To develop a more realistic constitutive model for the nanocomposite plate, this study integrates experimentally derived hyperelastic parameters of GPL–epoxy nanocomposites into a nonlinear plate vibration model governed by a Mooney–Rivlin strain-energy formulation. Following the derivation of the nonlinear governing equations of motion via Hamilton's principle, Galerkin's method is applied to discretize the system. The effective mechanical properties of the nanocomposite are obtained through experimental tensile testing performed on specimens containing varying concentrations of graphene nanoplatelets. Subsequently, the discretized equations are solved numerically to characterize the nonlinear dynamic behavior of the system. To this end, the influence of key parameters on various nonlinear phenomena is assessed using time-history responses, phase-plane portraits, Poincaré maps, and frequency-response curves. The

experimentally calibrated analytical–numerical methodology avoids arbitrary hyperelastic-parameter assumptions and enables direct transfer of the measured GPL-dependent nonlinear material behavior into the vibration model. The results demonstrate that increasing the GPL content up to 1.0 wt.% increases the resonant frequency by 57.9% and reduces the maximum vibration amplitude by 50% compared with pure epoxy. Furthermore, the formulation captures a softening-to-hardening transition governed by the competition between Mooney–Rivlin material nonlinearity and von Kármán membrane stretching. Accounting for hyperelastic material behavior is shown to be crucial for accurately predicting the dynamic response, particularly at larger amplitudes, where linear elastic models overestimate deflections.

Keywords: Nonlinear vibration; graphene nanoplatelets; hyperelastic behavior; tensile testing; Poincaré map.

Abbreviations

Abbreviation	Definition
ASTM	American Society for Testing and Materials
ASTM D638-IV	ASTM D638 Type IV tensile specimen standard
AUTO	Numerical continuation and bifurcation analysis software
DS	Initial continuation step size in AUTO
DSMAX	Maximum continuation step size in AUTO
DSMIN	Minimum continuation step size in AUTO
EPS	Residual convergence tolerance in AUTO
EPSL	Convergence tolerance for the Newton iteration equations in AUTO
EPSU	Convergence tolerance for the solution update in AUTO
FK20	Commercial epoxy resin system used as the matrix material
GPL	Graphene nanoplatelet
GPL-R	Graphene nanoplatelet-reinforced
NCOL	Number of collocation points per mesh interval in AUTO
NTST	Number of mesh intervals in AUTO
SEM	Scanning electron microscopy
wt.%	Weight percentage

1. Introduction

The increasing use of lightweight polymer-based structures in dynamically loaded engineering systems has created a strong need for materials and models capable of predicting vibration response beyond the assumptions of classical linear elasticity [1]. However, polymers typically exhibit lower strength and thermal resistance compared to other materials. This necessitates their reinforcement with other materials, including nanomaterials possessing unique properties [2]. High-strength nanomaterials, characterized by high thermal stability, desirable electrical conductivity, and robust chemical resistance, can impart enhanced electrical, thermal, and mechanical properties to polymer nanocomposites, extending their service life and thereby mitigating waste and environmental concerns [3]. Consequently, understanding the vibration behavior of polymer nanocomposite plates is essential not only for improving stiffness-to-weight performance, but also for controlling resonance, reducing large-amplitude oscillations, and preventing instability under time-dependent excitation. A central scientific challenge in this field is to determine how nanoscale reinforcement modifies the nonlinear constitutive response of the polymer matrix and, in turn, changes the global nonlinear vibration characteristics of the plate. At the material-characterization scale, recent studies on nanoindentation inverse analysis, indentation-based reverse identification of film/substrate cohesion, and moisture-sensitive polymer-modified layered minerals have shown that reliable prediction of mechanical response requires experimentally grounded parameter identification and careful consideration of microstructure-dependent material behavior [4-6].

The escalating use of compliant materials, such as polymers, elastomers, and rubbers, in diverse engineering applications necessitates a departure from traditional linear elastic models. These materials routinely experience substantial nonlinear strains within their elastic regimes, rendering conventional linear continuum mechanics inadequate for precise behavioral prediction. Consequently, a robust hyperelastic formulation is imperative for

accurate characterization. Prior research has focused on characterizing idealized soft structures without porosity and geometric imperfections, motivated by their growing applications in soft robotics [7], minimally invasive surgical instruments [8], and bio-integrated devices, including synthetic organs and implants. Hamilton's principle and Kirchhoff–Love plate theory are commonly used theoretical tools in nonlinear dynamics [9, 10]. The nonlinear mechanical characteristics of hyperelastic plates [11] and shells [12] have been extensively investigated employing strain-energy density models based on Ogden and Neo-Hookean formulations. These studies have consistently demonstrated a high degree of correlation between hyperelastic model predictions and experimental observations. From an engineering viewpoint, GPL-reinforced polymer plates represent a class of lightweight compliant structural components that may operate under repeated dynamic excitation, localized actuation, vibration transmission, or additional inertial effects. In such conditions, the critical design question is not only whether GPLs increase the small-strain stiffness of the polymer matrix, but how the GPL-induced changes in nonlinear constitutive behavior affect resonance frequency, vibration amplitude, jump phenomena, and stability of the forced response. This issue is scientifically important because the dynamic response of a hyperelastic plate is governed by a competition between material nonlinearity associated with the strain-energy function and geometric nonlinearity caused by large-deflection membrane stretching. Therefore, the main objective of this work is to determine how GPL concentration, through its effect on the experimentally measured Mooney–Rivlin constants, modifies the nonlinear vibration mechanisms of fully clamped polymer plates subjected to harmonic point excitation and concentrated mass. The resulting trends are intended to provide design guidance for controlling resonance, limiting large-amplitude oscillations, and tailoring nonlinear dynamic characteristics in lightweight GPL-reinforced polymer structures.

The study of nonlinear vibrations in thin hyperelastic plates involves understanding the complex interplay between material and geometric

nonlinearities. These plates, often made from materials like rubber or biological tissues, exhibit significant nonlinear behavior due to their hyperelastic nature. The research primarily focuses on modeling these nonlinearities using various hyperelastic material laws and analyzing the dynamic response of the plates under different conditions. Hyperelastic materials are characterized by their nonlinear stress-strain relationships, which are typically modeled using constitutive laws such as the Mooney-Rivlin model, the Neo-Hookean model, or the Ogden model. These models are essential for capturing the large deformations and nonlinear material behavior of hyperelastic plates. For instance, the Mooney-Rivlin model is widely used due to its ability to describe the nonlinear elastic response of rubber-like materials, as demonstrated in studies on nonlinear acoustic radiation from hyperelastic plates [13]. Similarly, the Neo-Hookean model has been employed to analyze the nonlinear vibrations of hyperelastic membranes and plates, particularly in the context of internal resonances and amplitude-dependent properties [14]. From a nonlinear-dynamics perspective, recent studies on bridge-deck vortex-induced vibration with multistability, bistable frequency responses of flow-filled graphene-reinforced pipes, and composite shells with embedded damping layers indicate that nonlinear resonance, jump response, and damping-dependent stability should be treated as design-relevant features rather than secondary effects [15-17].

Prior investigations have explored the complexities of hyperelastic material behavior in structural components, with a focus on nonlinear vibrations and dynamic response. Zheng et al. [11] derived governing equations for cylindrical shells under radial excitation, while Xie et al. [13] numerically analyzed rubber plates using finite element methods and the Mooney-Rivlin model. The influence of viscoelastic media on thin-plate vibrations, particularly the impact of damping characteristics, was investigated by Shitikova et al. [18]. Karimi et al. [19] focused on the nonlinear behavior of hyperelastic membranes embedded in elastic

foundations, using the Neo-Hookean model. Hosseini et al. [20] presented a static analysis of hyperelastic plates under various loading scenarios, employing higher-order plate theories and nonlinear strain relations. These diverse studies collectively underscore the importance of considering both material and geometric nonlinearities when analyzing the dynamic behavior of structures composed of hyperelastic materials. Parhi and Roy [21, 22] investigated chaotic vibration in auxetic carbon-nanotube-reinforced nanocomposite structures and showed that time histories, phase portraits, Poincaré maps, bifurcation diagrams, and jump phenomena are essential tools for characterizing nonlinear vibration behavior. Similarly, nonlinear vibration and energy-absorption responses of auxetic sandwich nanocomposite structures have been examined, demonstrating the relevance of negative-Poisson's-ratio configurations for vibration mitigation and energy dissipation. More recently, nonlinear dynamic studies of FG-GFRC-NPR structures and auxetic graded nanotube-reinforced polymeric composite beams have highlighted the need for nonlinear formulations when dealing with functionally graded, nanoreinforced, and energy-absorbing polymeric composite systems [23, 24]. These recent contributions confirm the growing interest in nonlinear vibration analysis of advanced nanocomposites; however, the experimentally calibrated hyperelastic vibration response of GPL-reinforced polymer plates remains insufficiently explored, which motivates the present study.

More broadly, the rapid development of nanotechnology across mechanical, biomedical, electronic, energy, and aerospace applications has intensified interest in nanoreinforced polymer systems whose multiscale properties can be tailored to enhance stiffness, stability, actuation capability, sensing performance, and vibration-control behavior [25, 26]. Recent advances in multilayer heterogeneous pyrocarbon composites, stainless-steel/copper composite strips, and graphene-skinned fibers further demonstrate that interfacial architecture, processing history, and nanoscale conductive skins can be used to tailor mechanical, thermal, electromagnetic,

and multifunctional performance of composite materials [27-29]. In the context of nonlinear vibration analysis of GPL-R structures, several recent studies have contributed significantly to the field [30-32]. The need for reliable dynamic models is also evident in complex mechanical systems such as herringbone planetary gears, high-pressure fuel-pump bush lubrication coupled with camshaft bending vibration, and pre-twisted mechanical-metamaterial sandwich blades, where geometric design, coupled motion, and structural configuration strongly influence vibration behavior [33-35]. Yang et al. [36] investigated the linear and nonlinear free vibrations of electrically prestressed highly aligned graphene-reinforced dielectric porous arches, considering large deformation and electrically induced stress. Yang et al. [36] examined the coupled dynamic instability of GPL-R dielectric porous arches under electromechanical loading, observing coupling effects between parametric and forced resonance. Fan and She [37] investigated the nonlinear transient response of graphene platelet-reinforced metal foams beams with initial geometric imperfections, providing valuable insights into the dynamic behavior of such composite systems under pulse loads. Subsequently, Fan et al. [38] extended this line of research to two-directional functionally graded spinning annular plates with variable thickness, examining the effects of spinning motion and geometric nonlinearity on their forced vibration characteristics. Fan et al. [39] analyzed the nonlinear transient response of revolution doubly curved shells reinforced with GPLs, considering initial geometric imperfections and porosity effects.

Multi-physics and rotating composite systems, including piezoelectric composites with cylindrical inhomogeneities, graphene-coated rotational blades under complex loads, and rotating dovetailed blades with flexible rough-contact connections, further demonstrate that anisotropy, graphene reinforcement, and boundary/interface conditions can substantially modify wave propagation and vibration characteristics [40-42]. Zhang et al. [43] investigated the aero-thermoelastic stability of GPL-reinforced nanocomposite lattice sandwich plates subjected to supersonic flow,

considering temperature- and moisture-dependent properties. Wang et al. [44] employed a nonlinear energy sink to suppress the nonlinear aeroelastic responses of GPL-reinforced composite lattice sandwich plates, demonstrating the effectiveness of passive control strategies in mitigating flutter. In the context of thermal environments, Wang and Zhang [45] examined the thermal buckling and postbuckling responses of temperature-dependent GPL-reinforced porous nanocomposite beams, revealing the crucial roles of porosity distribution and GPL dispersion patterns on thermal stability. Ma et al. [46] investigated the nonlinear thermal flutter behavior of GPL-R metal foam arbitrary quadrilateral plates under supersonic airflow, considering different temperature rise modes and employing the generalized differential quadrature method. More recently, She et al. [47] examined the geometrically nonlinear transient response of such quadrilateral plates under blast loads, taking into account the effects of viscoelastic foundations and thermal environments. Cheng and She [48] investigated the nonlinear transient response of rotating graphene-reinforced metal foam beams with cracks, considering the combined effects of rotational motion, material porosity, and geometric imperfections. More recently, the nonlinear internal resonance of graphene-reinforced metal foam plates with initial geometric imperfection under non-uniform temperature fields has been examined [49], revealing complex energy transfer mechanisms between modes under thermal environments. These studies underscore the importance of accounting for various practical factors—such as cracks, rotation, temperature fields, and geometric imperfections—in the accurate prediction of nonlinear dynamic behavior of the plates.

The reviewed literature indicates that three relevant research streams have been developed in parallel: nonlinear vibration analysis of hyperelastic plates and shells, dynamic modeling of GPL-R structures, and experimental characterization of polymer nanocomposites. However, the intersection of these topics remains insufficiently clarified, particularly for polymer plates in which the nonlinear constitutive response is governed by experimentally

identified hyperelastic parameters rather than assumed linear elastic or homogenized properties. In this context, an important knowledge gap concerns how GPL-dependent Mooney–Rivlin material parameters influence the forced nonlinear vibration response, resonance shift, amplitude reduction, and softening-to-hardening transition of hyperelastic polymer plates.

The present study addresses this observed gap by integrating tensile-test-derived Mooney–Rivlin constants into a Kirchhoff–Love/von Kármán plate formulation and by solving the resulting nonlinear equations using Galerkin discretization and numerical continuation. This framework enables direct assessment of the coupled effects of GPL concentration, experimentally calibrated material nonlinearity, geometric nonlinearity, and concentrated mass on the nonlinear dynamic response. The main contributions of the study are therefore: (i) incorporation of experimentally identified hyperelastic constants of GPL–epoxy nanocomposites into nonlinear plate vibration analysis; (ii) formulation of the forced vibration problem using a Mooney–Rivlin hyperelastic model combined with von Kármán geometric nonlinearity; (iii) identification of the mechanisms governing the transition from softening-type to hardening-type response; and (iv) provision of quantitative design-oriented results showing that 1.0 wt.% GPLs increases the resonant frequency by 57.9% and reduces the maximum vibration amplitude by 50% compared with pure epoxy. These contributions provide a constructive basis for designing lightweight GPL-R polymer plates with tailored nonlinear vibration characteristics. Thus, the scientific interest of the present problem lies in identifying how material-level changes introduced by GPL reinforcement are transferred to system-level nonlinear vibration features such as resonance shift, amplitude limitation, jump response, and stability variation.

2. Experimental Determination of Nanocomposite Mechanical Properties

In this study, FK20 resin was employed as the matrix material for fabricating graphene nanoplatelet (GPL)-reinforced nanocomposite samples. This matrix is a two-component resin based on Epoxy Bisphenol A and a Polyamine Hardener curing agent. The resin has a density of 1150 kg/m^3 and the two components are mixed at a weight ratio of 2:1. The graphene nanoplatelets, with a stated purity of 99.5%, were sourced from US-NANO (USA). A scanning electron microscope (SEM) image of the GPLs is presented in Figure 1.

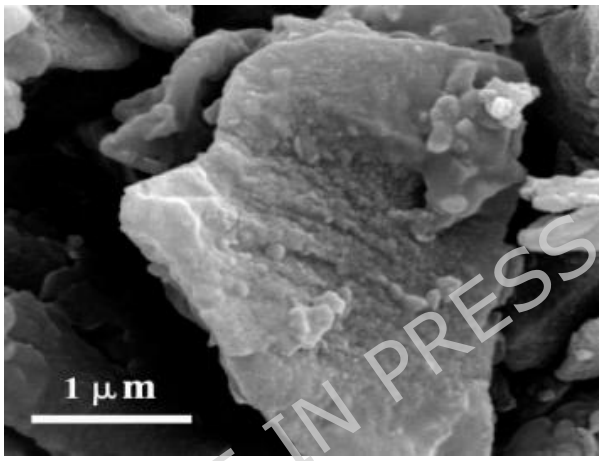

Figure 1: SEM image of the GPLs used in this study

GPL-reinforced epoxy nanocomposite specimens were fabricated using a direct mixing route designed to improve nanoparticle dispersion and reduce void formation. First, the required amount of GPLs (0, 0.2, 0.4, 0.6, 0.8, and 1 wt.%) was weighed according to the target weight fraction and gradually added to the FK20 epoxy resin. The mixture was mechanically stirred for 1 h at 1500 rpm to achieve initial distribution of the GPLs within the resin. Subsequently, the suspension was subjected to ultrasonication for 40 min using an ultrasonic bath in order to disrupt possible GPL agglomerates and improve nanoparticle dispersion. Since excessive temperature rise during sonication may change the resin viscosity and adversely affect the curing process, an ice-water bath was used to maintain a low mixture temperature, and the suspension was allowed to rest for 3 min after every 10 min of ultrasonication. The mixture was then degassed under vacuum for 20 min to

remove entrapped air bubbles. Afterward, the hardener was added according to the prescribed resin-to-hardener mixing ratio, and the mixture was gently stirred for 5 min to avoid additional air entrapment. A second vacuum degassing step was performed for 10 min before casting. Finally, the mixture was poured into molds conforming to the ASTM D638-IV tensile specimen geometry, cured for 3 h at 85°C, and post-cured for 1 h at 110°C. The specimens were then stored at room temperature for one week to ensure complete curing, and surface irregularities were removed using fine sandpaper before testing.

Direct tensile testing was performed using a Zwick-Z250 universal testing machine with a capacity of 10 kN and an accuracy of 0.2%, and the measured load–displacement data were converted into stress–strain curves for each GPL concentration. Displacement-controlled loading was applied at a rate of 10 mm/min, and testing continued until specimen failure. Additionally, an extensometer with a resolution of 1 µm was used, as shown in Figure 2c, to accurately measure the local strain in the gauge section and to reduce errors associated with machine compliance during extraction of the stress–strain curves.

The mechanical characterization followed an experimental-to-constitutive modelling procedure. For each GPL concentration, the force and displacement data recorded during the ASTM D638-IV tensile test were converted into stress–strain curves using the initial specimen geometry and the strain measured by the extensometer. The use of the extensometer was important because it reduced errors associated with machine compliance and provided a more reliable measurement of the local strain in the gauge section. The resulting stress–strain curves were used to determine the small-strain stiffness, tensile strength, fracture strain, and, more importantly, the nonlinear material response required for hyperelastic parameter identification. Therefore, the tensile tests provided the direct experimental basis for calibrating the GPL-dependent material model used in the subsequent nonlinear vibration analysis.

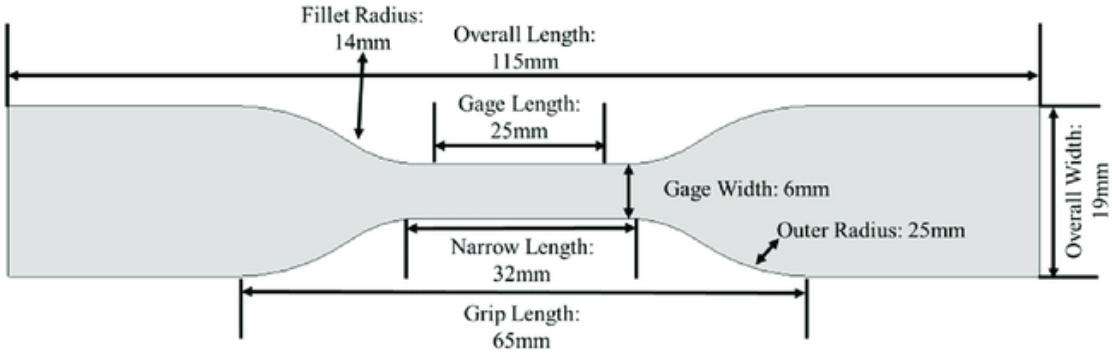

(a)

(b) (c)

Figure 2: (a) Geometric dimensions of the direct tensile test specimen according to ASTM D638-IV, (b) nanocomposite samples containing various GPL concentrations, and (c) experimental setup for the direct tensile test.

Uniform dispersion of GPLs is a critical requirement for obtaining reliable GPL-reinforced polymer nanocomposites. When the nanoplatelets are uniformly distributed in the epoxy matrix, their large interfacial area can contribute effectively to load transfer, restriction of polymer chain mobility, and enhancement of stiffness. In contrast, agglomerated GPL clusters reduce the effective reinforcing surface area and introduce local stress concentration zones, which may initiate premature damage and reduce the tensile strength and fracture strain. Nonuniform dispersion also produces

spatial variations in local stiffness and tangent material response. Therefore, dispersion quality directly affects the measured stress–strain curves and the Mooney–Rivlin constants extracted from them. Because these experimentally identified constants are subsequently used in the nonlinear vibration model, achieving a representative dispersion state is essential for accurate prediction of resonance frequency, vibration amplitude, and nonlinear response characteristics.

3. Hyperelastic Constitutive Relationships

To provide a clear overview of the integrated approach adopted in this study—combining experimental characterization, constitutive modeling, and nonlinear vibration analysis—a schematic flowchart is presented in Figure 3. This flowchart outlines the sequential steps from material fabrication and tensile testing to the extraction of hyperelastic constants, theoretical formulation, discretization, numerical solution, and parametric analysis. The present section focuses on the hyperelastic constitutive relationships, which form the core of the material modeling. Following the experimental determination of the Mooney–Rivlin coefficients (C_1 and C_2) described in Section 2, the theoretical framework for the hyperelastic plate is developed herein.

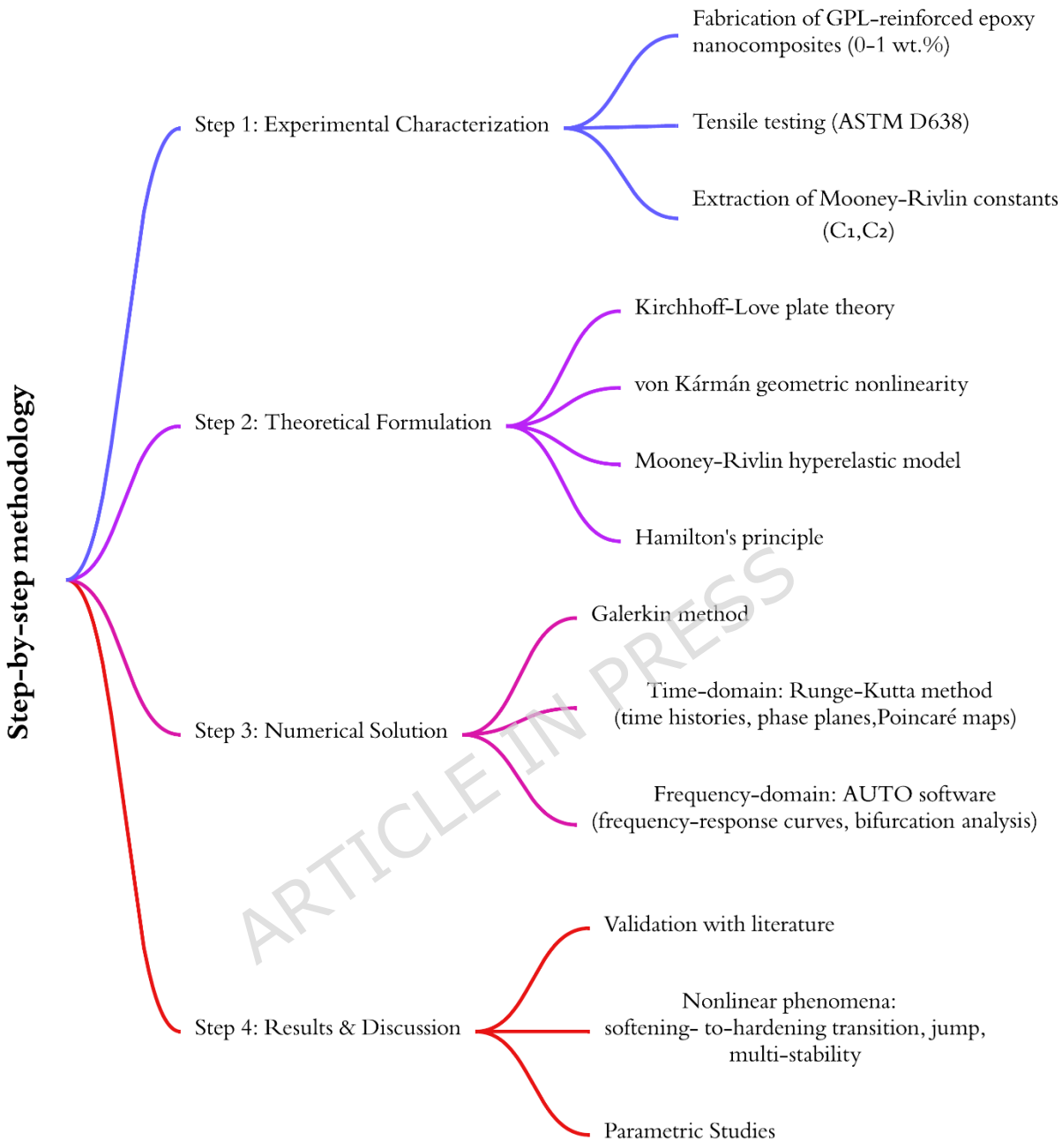

Figure 3: Schematic flowchart illustrating the step-by-step methodology of the present study

The use of a hyperelastic constitutive model is essential for GPL-reinforced polymer plates because these structures cannot be accurately represented as linear elastic plates with only a modified Young's modulus. In a linear elastic model, the stress is assumed to be proportional to strain and

the stiffness remains constant during deformation. Such an approximation is valid only in the infinitesimal-strain regime. In contrast, epoxy-based nanocomposites reinforced with GPLs may exhibit strain-dependent tangent stiffness due to the nonlinear response of the polymer matrix, the restriction of polymer chain mobility by GPLs, and interfacial deformation mechanisms between the matrix and the nanoplatelets. Under large transverse deflections, the plate also experiences membrane stretching and localized shear near the clamped boundaries. Therefore, the overall response is governed by the coupling between material nonlinearity and von Kármán geometric nonlinearity. A hyperelastic strain-energy formulation, such as the Mooney–Rivlin model, enables this deformation-dependent energy storage to be described through the strain invariants and allows the experimentally identified material constants to be directly incorporated into the nonlinear vibration model.

The stress–strain response of GPL-reinforced polymer nanocomposites is generally nonlinear and strain-dependent; therefore, a traditional linear elastic model with a constant Young's modulus cannot adequately represent the evolving stiffness and strain-energy storage of the material under finite deformation. The stress-strain behavior of soft polymer structures should be experimentally characterized to determine their hyperelastic material parameters. Strain-energy density models, which have shown a respectable level of accuracy in simulating isotropic soft materials, are used to represent the constitutive behavior of these materials due to their nonlinear stress-strain behavior. The nonlinear elasticity of rubbers and polymeric materials is typically described by hyperelastic constitutive laws, and these materials are often assumed to be incompressible. Commonly, three hyperelastic models are considered, along with their associated strain-energy density function, W [50]:

Neo-Hookean:

$$W = \frac{E}{6}(I_1 - 3) \quad (1)$$

Mooney-Rivlin:

$$W = \frac{C_1}{2}(I_1 - 3) + \frac{C_2}{2}(I_2 - 3) \quad (2)$$

Ogden:

$$W = \sum_{i=1}^{N} \frac{C_i}{\alpha_i}\left(I_1^{\alpha_i} + I_2^{\alpha_i} + I_3^{\alpha_i} - 3\right) \quad (3)$$

where:

- I_1 is the first invariant of the right Cauchy-Green deformation tensor, **B**.
- E is elastic modulus of the plate.
- I_2 is second invariant of the right Cauchy-Green deformation tensor.
- λ_1, λ_2, and λ_3 are the principal stretches of the plate.
- C_i and α_i denote material parameters.

The use of a hyperelastic constitutive model is essential for GPL-reinforced polymer plates because these structures cannot be accurately represented as linear elastic plates with only a modified Young's modulus. In a linear elastic model, the stress is assumed to be proportional to strain and the stiffness remains constant during deformation. Such an approximation is valid only in the infinitesimal-strain regime. In contrast, epoxy-based nanocomposites reinforced with GPLs may exhibit strain-dependent tangent stiffness due to the nonlinear response of the polymer matrix, the restriction of polymer chain mobility by GPLs, and interfacial deformation mechanisms between the matrix and the nanoplatelets. Under large transverse deflections, the plate also experiences membrane stretching and localized shear near the clamped boundaries. Therefore, the overall response is governed by the coupling between material nonlinearity and von Kármán geometric nonlinearity. A hyperelastic strain-energy formulation, such as the Mooney–Rivlin model, enables this deformation-dependent energy storage to be described through the strain invariants and allows the experimentally identified material constants to be directly incorporated into the nonlinear vibration model.

Among the available hyperelastic constitutive models, the Neo-Hookean, Mooney–Rivlin, and Ogden formulations are widely used, but they differ significantly in the number of material parameters, fitting flexibility, calibration robustness, and suitability for nonlinear vibration analysis. The Neo-Hookean model offers simplicity and low computational cost because it uses a single material parameter; however, its dependence only on the first invariant limits its ability to capture strain-induced stiffening and shear-sensitive nonlinear response at larger deformations. The Ogden model is highly flexible for complex large-strain responses, but its multiple parameters require richer experimental data for unique calibration and may introduce unnecessary numerical complexity in the present analytical–numerical vibration formulation. The Mooney–Rivlin model, with two experimentally identifiable constants C_1 and C_2, provides the best balance between fitting accuracy, parameter-identification robustness, and mathematical tractability for GPL-reinforced polymer plates. It reliably captures the nonlinear stress–strain response up to moderate-to-large deformations while allowing robust parameter identification from standard tensile tests. Accordingly, the Mooney–Rivlin model is adopted in this study, as it is well-suited for the expected strain levels in hyperelastic plates and has been validated in prior investigations [51].

The effective material properties of the GPL-R nanocomposite were directly extracted from the experimental stress–strain data obtained from tensile tests on specimens with varying GPL concentrations (0, 0.2, 0.4, 0.6, 0.8, and 1.0 wt.%). For each concentration, the Mooney–Rivlin hyperelastic model constants C_1 and C_2 were determined by fitting the experimental stress–strain curve using a nonlinear least-squares regression. The fitting procedure minimizes the error between the experimental Cauchy stress and the theoretical stress predicted by the Mooney–Rivlin model:

$$s_{\text{theory}} = 2\left(C_1 + \frac{C_2}{I}\right)\left(\lambda - \frac{1}{\lambda^2}\right) \quad (4)$$

where $\lambda=1+\varepsilon$ is the stretch ratio. The optimization was performed using the Levenberg–Marquardt algorithm, with the goodness of fit quantified by the coefficient of determination ($R^2>0.99$ for all concentrations). These experimentally calibrated constants were then directly employed in the nonlinear vibration analysis, ensuring that the material model accurately reflects the actual mechanical behavior of the nanocomposite without recourse to homogenization or micromechanical approximations. This approach captures not only the stiffening effect of GPLs but also the intrinsic nonlinearity of the polymer matrix, which is essential for accurate prediction of large-amplitude vibrations.

3.1 Hyperelastic Nanocomposite Plate Model

This study investigates the nonlinear vibrations of a rectangular flexible plate with length a, width b, and thickness h. The plate is composed of a GPL-R polymer. The plate is fully clamped along all edges, and a concentrated mass, M_{mass}, is located at position (x_{mass}>, y_{mass}). All numerical results reported in this study correspond to this fully clamped boundary condition. The plate is also subjected to a harmonic concentrated force, $F(t) = F_0 sin(\omega t)$, acting at position (x_{force}, y_{force}) (Figure 4). Because the GPL-reinforced polymer plate may experience finite elastic strains during large-amplitude transverse vibration, a hyperelastic constitutive model is employed to capture the nonlinear stress–strain response and the deformation-dependent stiffness of the nanocomposite.

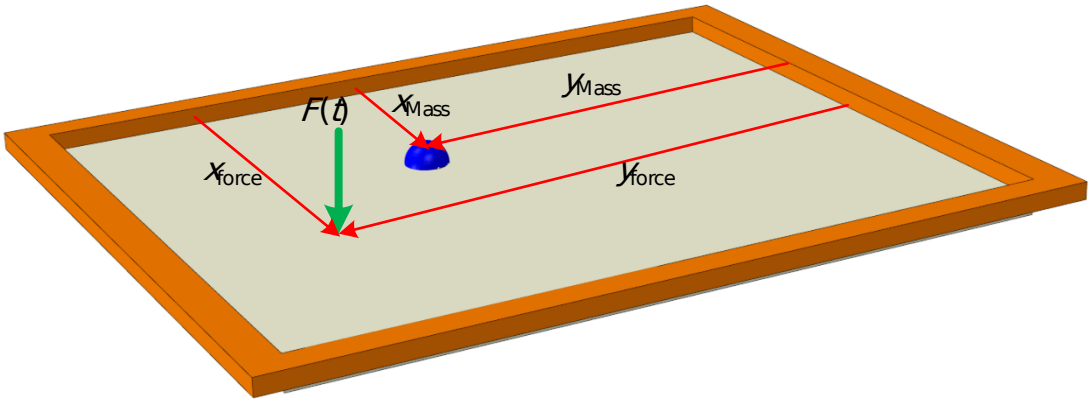

Figure 4: Plan of a hyperelastic nanocomposite plate with fully clamped supports subjected to a point force and a concentrated mass.

For hyperelastic nanocomposite plate with geometric dimensions illustrated in Figure 4, deformation gradient tensor **F** and left Cauchy-Green deformation tensor **B** are defined as [52]:

$$\mathbf{F}=\begin{bmatrix}1+e_x & e_{xy} & 0\\ e_{xy} & 1+e_y & 0\\ 0 & 0 & 1+e_z\end{bmatrix} \quad (5a)$$

$$\mathbf{B}=\mathbf{F}^T\mathbf{F}=\begin{bmatrix}(1+e_x)^2+e_{xy}^2 & (2+e_x+e_y)e_{xy} & 0\\ (2+e_x+e_y)e_{xy} & (1+e_y)^2+e_{xy}^2 & 0\\ 0 & 0 & (1+e_z)^2\end{bmatrix} \quad (5b)$$

where ε_x, ε_y, and ε_z are the axial strains, and ε_{xy} stands in-plane shear strain, which, for a Kirchhoff–Love plate, are defined as [53]:

$$e_x=\frac{\partial u(x,y)}{\partial x}-z\frac{\partial^2 w(x,y)}{\partial x^2}+\frac{1}{2}\left(\frac{\partial w(x,y)}{\partial x}\right)^2 \quad (6a)$$

$$e_y=\frac{\partial v(x,y)}{\partial y}-z\frac{\partial^2 w(x,y)}{\partial y^2}+\frac{1}{2}\left(\frac{\partial w(x,y)}{\partial y}\right)^2 \quad (6b)$$

$$e_{xy}=\frac{\partial u(x,y)}{\partial y}+\frac{\partial v(x,y)}{\partial x}-2z\frac{\partial^2 w(x,y)}{\partial x\partial y}+\frac{\partial w(x,y)}{\partial x}\frac{\partial w(x,y)}{\partial y} \quad (7)$$

Here, the displacements in the x, y, and z directions are denoted by the letters u, v, and w, respectively. Using Eqs. (5)–(7), the first two invariants of the left Cauchy–Green strain tensor can be expressed as follows [54]:

$$I_1 = \mathrm{tr}(\mathbf{B}) = 3 + 2\left(e_z + e_y + e_x\right) + e_x^{\,2} + e_y^{\,2} + e_z^{\,2} + 2e_{xy}^{\,2} \quad (8)$$

$$\begin{aligned} I_2 = \frac{1}{2}\left(\mathrm{tr}(\mathbf{B})^2 - \mathrm{tr}\left(\mathbf{B}^2\right)\right) &= 3 + 4\left(e_z + e_y + e_x\right) + 2\left(e_x^{\,2} + e_y^{\,2} + e_z^{\,2}\right) \\ &+ 4\left(e_x e_y + e_x e_z + e_y e_z\right) + 2\left(e_x^{\,2} e_y + e_x^{\,2} e_z + e_x e_y^{\,2} + e_y^{\,2} e_z + e_x e_z^{\,2}\right) \\ &+ 2\left(e_y e_z^2 + 2e_{xy}^{\,2} e_z - e_{xy}^{\,2} e_y - e_{xy}^{\,2} e_x\right), \end{aligned} \quad (9)$$

Considering the incompressibility condition, $I_3 = \det(\mathbf{B}) = 1$ [54], the following compatibility relation is obtained:

$$e_z = -e_x - e_y + 2\left(e_x^2 + e_y^2 + e_x e_y + e_{xy}^2\right) + 16\left(e_x^2 e_y + e_y^2 e_x - e_{xy}^2 e_x - e_{xy}^2 e_y\right) \quad (10)$$

This study makes use of the Mooney-Rivlin hyperelastic strain-energy density model. Accordingly, the strain invariants within the framework of the Mooney-Rivlin hyperelastic strain-energy density model can be used to model strain energy of an incompressible hyperelastic nanocomposite plate based on Eq. (2) as [55]:

$$W = C_1(I_1 - 3) + C_2(I_2 - 3) \quad (11)$$

in which C_1 and C_2 stand material coefficients of Mooney-Rivlin hyperelastic model. The hyperelastic material parameters C_1 and C_2 used in the strain energy function (Eq. 11) are those determined experimentally in Section 4.1 (Table 1).

Considering the nonzero strain fields, the variation of the potential energy of the plate can be expressed as:

$$\begin{aligned}\delta PE = \int_A \{ & \left[6C_1\left(2\varepsilon_x + \varepsilon_y - 2\varepsilon_x^2 + 8\varepsilon_x\varepsilon_y + 4\varepsilon_y{}^2 - 6\varepsilon_{xy}^2\right)\right. \\ & \left. + 8C_2\left(2\varepsilon_x + \varepsilon_y + 20\varepsilon_x\varepsilon_y + 10\varepsilon_y^2 - 10\varepsilon\varepsilon_{xy}^2\right)\right]\delta\varepsilon_x \\ & + \left[6C_1\left(2\varepsilon_y + \varepsilon_x - 2\varepsilon_y^2 + 4\varepsilon_x^2 + 8\varepsilon_x\varepsilon_y - 6\varepsilon_{xy}^2\right)\right. \\ & \left. + 8C_2\left(2\varepsilon_y + \varepsilon_x + 10\varepsilon_x^2 + 20\varepsilon_x\varepsilon_y - 10\varepsilon_{xy}^2\right)\right]\delta\varepsilon_y \\ & + \left[12C_1\left(\varepsilon_{xy} - 6\varepsilon_x\varepsilon_{xy} - 6\varepsilon_y\varepsilon_{xy}\right)\right. \\ & \left. + 16C_2\left(\varepsilon_{xy} - 8\varepsilon_x\varepsilon_{xy} - 8\varepsilon_y\varepsilon_{xy}\right)\right]\delta\varepsilon_{xy}\}dAdx\end{aligned} \quad (12)$$

Additionally, the kinetic energy of the hyperelastic nanocomposite plate with a concentrated mass (M_{mass}) is:

$$\begin{aligned}T = & \frac{1}{2}\int_V \rho\left[\left(u_t - zw_{xt}\right)^2 + \left(v_t - zw_{yt}\right)^2 + w_t^2\right]dV \\ & + \frac{1}{2}\int_0^a\int_0^b M_{mass}\left[u_t^2 + v_t^2 + w_t^2\right]\delta\left(y - y_{mass}\right)\delta\left(x - x_{mass}\right)dxdy\end{aligned} \quad (13)$$

where ρ is the density of the nanocomposite plate.

Assuming that the plate is subjected to an external concentrated force, F, the external work done by the applied force is:

$$W_F = \int_0^a\int_0^b F(t)\delta\left(y - y_{force}\right)\delta\left(x - x_{force}\right)dxdy \quad (14)$$

Given the strain energy, kinetic energy, and work done by external forces, Hamilton's principle is employed to derive the governing equations of motion. Hamilton's principle is stated as [56, 57]:

$$\delta\int_{t_1}^{t_2}\left(T - U + W_f\right)dt = 0 \quad (15)$$

By applying Hamilton's principle and performing the mathematical derivations, the following nonlinear coupled equations of motion for the GPL-reinforced hyperelastic nanocomposite plate are obtained:

$$
\begin{aligned}
&\left(r + M_{mass}\,d(y - y_{mass})\,d(x - x_{mass})\right)u_{tt} - (3C_1 + 4C_2)\left(4u_{xx} + u_{yy} - 3v_{xy}\right) \\
&\quad + 12C_1\frac{\partial}{\partial x}\left(u_x^2\right) + \frac{1}{4}(36C_1 + 70C_2)\left(u_y^2\right)_x + (18C_1 + 35C_2)\left(u_y u_x\right)_y \\
&- 14(4C_1 + 10C_2)\left(u_x v_y\right)_x + (18C_1 + 35C_2)\left(\left(u_y v_x\right)_x + \left(u_y v_y\right)_y + \left(u_x v_x\right)_y\right) \\
&- (24C_1 + 70C_2)\left(v_y^2\right)_x + (18C_1 + 35C_2)\left(\frac{1}{2}\left(v_x^2\right)_x + \left(v_x v_y\right)_y\right) \\
&- (3C_1 + 4C_2)\left(\left(w_y^2\right)_x - \left(w_x w_y\right)_y\right) + C_1 h^2\left(w_{xx}^2\right)_x - (6C_1 + 8C_2)\left(w_x^2\right)_x \\
&- \frac{1}{12}(24C_1 + 70C_2)\,h^2\left(\left(w_{yy}^2\right)_x - 2\left(w_{xx} w_{yy}\right)_x + \left(w_{xy}^2\right)_x + \left(w_{xx} w_{xy}\right)_y\right) \\
&+ \frac{1}{6}(18C_1 + 35C_2)\,h^2\left(w_{xy} w_{yy}\right)_y + 12C_1\left(u_x w_x^2\right)_x - (24C_1 + 70C_2)\left(u_x w_y^2\right)_x \\
&+ (18C_1 + 35C_2)\left(\left(u_y w_x w_y\right)_x + \left(u_x w_x w_y\right)_y + \frac{1}{2}\left(u_y w_x^2\right)_y + \frac{1}{2}\left(u_y w_y^2\right)_y\right) \\
&- (24C_1 + 70C_2)\left(\left(v_y w_y^2\right) - \left(v_y w_x^2\right)\right)_x + 3C_1\left(w_x^4\right)_x \\
&+ (18C_1 + 35C_2)\left(\left(v_x w_x w_y\right)_x + \frac{1}{2}\left(v_x w_x^2\right)_y + \frac{1}{2}\left(v_x w_y^2\right)_y + \left(v_y w_x w_y\right)_y\right) \\
&- \frac{1}{2}(12C_1 + 35C_2)\left(w_y^4\right)_x + \frac{1}{2}(18C_1 + 3C_2 - C_2)\left(w_x^2 w_y\right)_y \\
&\quad - \frac{1}{2}(6C_1 + 3C_2)\left(w_x^2 w_y^2\right)_x + \frac{1}{2}(18C_1 + 35C_2)\left(w_x w_y^3\right)_y = 0
\end{aligned}
\tag{16}
$$

$$
\begin{aligned}
&\left(r + M_{mass}\,d(y - y_{mass})\,d(x - x_{mass})\right)v_{tt} - (3C_1 + 4C_2)\left(3u_{xy} + 4v_{yy} + v_{xx}\right) \\
&+(18C_1 + 35C_2)\left(\frac{1}{2}\left(u_y^2\right)_y + \left(u_x u_y\right)_x + \left(u_y v_x\right)_y + \left(u_x v_x\right)_x\right) \\
&-(24C_1 + 70C_2)\left(2\left(u_x v_y\right)_y + \left(u_x^2\right)_y\right) + 12C_1\left(v_y^2\right)_y + (18C_1 + 35C_2)\left(\left(u_y v_y\right)_x + \frac{1}{2}\left(v_x^2\right)_y\right) \\
&-\frac{1}{12}(24C_1 + 70C_2)h^2\left(2w_y w_x + w_x^2\right)_y - (3C_1 + 4C_2)\left(w_w w_w\right)_x \\
&+\frac{1}{12}(36C_1 + 70C_2)h^2\left(w_w^2\right)_y + \frac{h^2}{6}(18C_1 + 3C_2)\left(w_w w_w\right)_x \\
&+\frac{1}{6}(18C_1 + 35C_2)h^2\left(w_y^2\right)_x + (12C_1)\left(w_2^2\right)_y - (24C_1 + 70C_2)\left(u_x w_x^2\right)_y \\
&+(18C_1 + 35C_2)\left(u_y w_x w_y\right)_x + 3C_1\left(w_y^4\right)_y - \frac{1}{4}(24C_1 + 7C_2)\left(w_x^4\right)_y \\
&-\frac{1}{4}(12C_1 + 70C_2)\left(w_x^2 w_y^2\right)_y + \frac{1}{2}(18C_1 + 3C_2)\left(w_x^2 w_y\right)_x + \frac{1}{2}(18C_1 + 35C_2)\left(w_x w_y^3\right)_x = 0
\end{aligned}
\tag{17}
$$

$$
\begin{aligned}
&\rho w_{tt} - \frac{1}{12}\rho h^2 w_{xxtt} - \frac{1}{12}\rho h^2 w_{yytt} + M_{\text{mass}}\,\delta(y - y_{\text{mass}})\,\delta(x - x_{\text{mass}})\,w_{tt} \\
&+\frac{1}{12}(12C_1 + 16C_2)h^2\left(w_{xxxx} + 2w_{xxyy} + w_{yyyy}\right) - 2C_1 h^2\left(u_x w_{xx}\right)_{xx} \\
&+\frac{1}{6}(24C_1 + 70C_2)h^2\left(u_x w_{yy}\right)_{xx} - \frac{1}{12}(36C_1 + 70C_2)h^2\left(u_y w_{xy}\right)_{xx} \\
&-(12C_1 + 16C_2)(u_x w_x)_x + \frac{1}{6}(24C_1 + 70C_2)h^2\left(u_x w_{xx}\right)_{yy} + \frac{1}{6}(24C_1 + 70C_2)h^2\left(u_x w_{yy}\right)_{yy} \\
&-\frac{1}{12}(36C_1 + 70C_2)h^2\left(u_y w_{xy}\right)_{yy} - (6C_1 + 8C_2)(u_x w_x)_y - \frac{1}{3}(18C_1 + 35C_2)h^2\left(u_x w_{xy}\right)_{xy} \\
&-\frac{1}{6}(18C_1 + 35C_2)h^2\left(u_y w_{xx}\right)_{xy} - \frac{1}{6}(18C_1 + 35C_2)h^2\left(u_y w_{yy}\right)_{xy} - (3C_1 + 4C_2)\left(u_y w_y\right)_x \\
&-(3C_1 + 4C_2)\left(u_y w_x\right)_y + \frac{1}{3}(18C_1 + 35C_2)h^2\left(v_y w_{yy}\right)_{xx} + \frac{1}{3}(12C_1 + 35C_2)h^2\left(v_y w_{xx}\right)_{xx} \\
&+\frac{1}{4}(36C_1 + 70C_2)\left(u_y^2 w_y\right)_y + (18C_1 + 35C_2)\left(u_x u_y w_y\right)_x + (18C_1 + 35C_2)\left(u_x u_y w_x\right)_y \\
&+\frac{1}{4}(36C_1 + 70C_2)\left(u_y{}^2 w_x\right)_x - (24C_1 + 70C_2)\left(v_y^2 w_x\right)_x - (24C_1 + 70C_2)\left(u_x w_x^2 w_y\right)_y \\
&+\frac{1}{2}(18C_1 + 35C_2)\left(\left(v_x^2 w_x\right)_x + \frac{1}{4}\left(v_x^2 w_y\right)_y + \left(u_y v_x w_x\right)_x + \left(u_y v_y w_x\right)_y\right) \\
&+(18C_1 + 35C_2)\left(v_x v_y w_y\right)_x + (18C_1 + 35C_2)\left(v_x v_y w_x\right)_y - (48C_1 + 140C_2)\left(u_x v_y w_x\right)_x \\
&+\frac{1}{2}(36C_1 + 70C_2)\left(u_y v_x w_y\right)_y + (18C_1 + 35C_2)\left(u_x v_x w_y\right)_x - (48C_1 + 140C_2)\left(u_x v_y w_y\right)_y \\
&+(18C_1 + 35C_2)\left(u_y v_y w_y\right)_x + (18C_1 + 35C_2)(u_x v_x w_x)_y + 12C_1\left(\left(u_x w_x^2\right)_x + \left(v_y^2 w_y\right)_y\right) \\
&-\frac{1}{2}(48C_1 + 140C_2)\frac{\partial}{\partial x}\left(u_x w_x w_y^2\right)_x + \frac{1}{2}(36C_1 + 70C_2)\frac{\partial}{\partial x}\left(u_y w_x^2 w_y\right)_x \\
&-\frac{1}{2}(48C_1 + 140C_2)\left(u_x w_y^3\right)_y + (18C_1 + 35C_2)\left(\left(u_y w_x w_y^2\right)_y + \left(u_x w_x w_y^2\right)_x\right)
\end{aligned}
$$

$$+\frac{1}{2}(18C_1+35C_2)\left((u_y w_x^2 w_y)_x+(u_y w_y^3)_x+2(u_x w_x^2 w_y)_y+(u_y w_x^3)_y+(v_y w_x w_y^2)_y\right)$$
$$12w_y^3-(24C_1+70C_2)\left((v_y w_x w_y^2)_x+(v_y w_x^2 w_y)_y\right)+\frac{1}{2}(36C_1+70C_2)(v_x w_x w_y^2)_y$$
$$-\frac{1}{2}(48C_1+140C_2)(v_y w_x^3)_x+\frac{1}{2}(36C_1+70C_2)(v_x w_x^2 w_y)_x+(18C_1+35C_2)(v_y w_x^2 w_y)_y$$
$$+\frac{1}{2}(18C_1+35C_2)\left((v_x w_x w_y^2)_y+(v_x w_x^3)_y+2(v_y w_x w_y^2)_x\right)+3C_1(w_y^5)_y+3C_1(w_x^5)_x \quad (18)$$
$$+\frac{1}{2}(18C_1+35C_2)\left((v_x w_y^3)_x+(v_x w_x^2 w_y)_x\right)-\frac{1}{4}(24C_1+70C_2)\left((w_x w_y^4)_x+(w_x^4 w_y)_y\right)$$
$$-\frac{1}{4}(12C_1+70C_2)\left((w_x^3 w_y^2)_x+(w_x^2 w_y^3)_y\right)+\frac{1}{2}(18C_1+35C_2)\left((w_x^3 w_y^2)_x+(w_x^2 w_y^3)_y\right)$$
$$+\frac{1}{2}(18C_1+35C_2)\left((w_x w_y^4)_x+(w_x^4 w_y)_y\right)=F(x,y,t)$$

The equations of motion of the hyperelastic nanocomposite plate obtained by neglecting Poisson's effect and the deformation in the y-direction are identical to those reported by Khaniki et al. [51]. The derived equations are validated by this correspondence.

3.2 Non-dimensionalization of Equations of Motion

To solve the coupled nonlinear equations of motion of the hyperelastic nanocomposite plate, the following non-dimensional parameters are defined:

$$x^*=\frac{x}{a},y^*=\frac{y}{b},x^*_{mass}=\frac{x_{mass}}{a},y^*_{mass}=\frac{y_{mass}}{b},x^*_{Force}=\frac{x_{Force}}{a},y^*_{Force}=\frac{y_{more}}{b},$$
$$z^*=\frac{z}{h},v^*=\frac{v}{h},w^*=\frac{w}{h},u^*=\frac{u}{h},A_1=\frac{C_1}{C_2},A_2=\frac{3C_1+4C_2}{C_2},M^*_{mass}=\frac{M_{mass}}{rA},$$
$$h_a=\frac{h}{a},h_b=\frac{h}{b},A_3=\frac{18C_1+35C_2}{C_2},A_4=\frac{24C_1+70C_2}{C_2},A_5=\frac{12C_1+70C_2}{C_2}, \quad (19)$$
$$F^*=\frac{Fa^2b^2}{C_2h^4},I=\sqrt{\frac{r_0a^2b^2}{C_2h^2}},\ t^*=t\frac{h}{ab}\sqrt{\frac{C_2}{r_0}},$$

Substituting the above non-dimensional parameters into the equations of motion (16)-(18), the equations of motion in terms of non-dimensional parameters are obtained as:

$$
\begin{aligned}
&\left(1+M_{\text{mass}}\,d(x-x_{\text{mass}})\,d(y-y_{\text{mass}})\right)u_{tt}-4\frac{A_2}{h_b^2}u_{xx}-\frac{A_2}{h_a^2}u_{yy}-3\frac{A_2}{h_a h_b}v_{xy}\\
&+12\frac{h_a}{h_b^2}A_1\left(u_x^2\right)_x+\frac{A_3}{2h_a}\left(u_y^2\right)_x+\frac{A_3}{h_a}\left(u_x u_y\right)_y-2\frac{A_4}{h_b}\left(u_x v_y\right)_x\\
&+\frac{1}{h_b}A_3\left(u_y v_x\right)_x+\frac{1}{h_b}A_3\left(u_x v_x\right)_y+\frac{h_b A_3}{h_a^2}\left(u_y v_y\right)_y-\frac{A_4}{h_a}\left(v_y^2\right)_x\\
&+\frac{1}{2}\frac{h_a^{\,2}}{h_b^{\,2}}\left(v_x^2\right)_x+\frac{1}{h_a}A_3\left(v_x v_y\right)_y-2\frac{h_a}{h_b^{\,2}}A_2\left(w_x^2\right)_x-\frac{1}{6}h_a A_4\left(w_{xx}w_{yy}\right)_x\\
&-\frac{1}{h_a}A_2\left(w_y^2\right)_x+\frac{h_a^{\,3}}{h_b A_1}\left(w_{xx}^{\,2}\right)_x-\frac{1}{12}\frac{h_b^{\,2}}{h_a}A_4\left(w_{yy}^{\,2}\right)_x+12\frac{h_a^{\,2}}{h_b^2}A_1\left(u_x w_x^2\right)_x\\
&+\frac{1}{6}h_a A_3\left(w_{xy}^{\,2}\right)_x-\frac{1}{h_a}A_2\left(w_x w_y\right)_y+\frac{1}{6}h_a A_3\left(w_{xx}w_{xy}\right)_y+\frac{1}{6}\frac{h_b^{\,2}}{h_a}A_3\left(w_{xy}w_{yy}\right)_y\\
&-A_4\left(u_x w_y^2\right)_x+A_3\left(u_y w_x w_y\right)_x+A_3\left(u_x w_x w_y\right)_y+\frac{1}{2}A_3\left(u_y w_x^2\right)_y\\
&+\frac{1}{2}\frac{h_b^{\,2}}{h_a^2}A_3\left(u_y w_y^2\right)_y-\frac{h_b}{h_a}A_4\left(v_y w_y^2\right)_x-\frac{h_a}{h_b}A_4\left(v_y w_x^2\right)_x+\frac{h_a}{h_b}A_3\left(v_x w_x w_y\right)_x\\
&+\frac{1}{2}\frac{h_a}{h_b}A_3\left(v_x w_x^2\right)_y+\frac{1}{2}\frac{1}{h_a}\frac{h_b}{A_3}\left(v_x w_y^2\right)_y+\frac{h_b}{h_a}A_3\left(v_y w_x w_y\right)_y+3\frac{h_a^{\,3}}{h_b^{\,2}}A_1\left(w_x^4\right)_x\\
&-\frac{1}{4}\frac{h_b^{\,2}}{h_a}A_4\left(w_y^4\right)_x-\frac{1}{4}h_a A_5\left(w_x^2 w_y^2\right)_x+\frac{1}{2}h_a A_3\left(w_x^3 w_y\right)_y+\frac{1}{2}\frac{h_b^{\,2}}{h_a}A_3\left(w_x w_y^3\right)_y=0
\end{aligned}
\tag{20}
$$

$$w_{tt} - \frac{1}{12}h_a^2(w_{ext}) + M_{mass}d(x - x_{mass})d(y - y_{mass})w_{tt} + cw_t + - \frac{1}{12}h_b^2(w_{yyt}) + \frac{1}{3}A_2\frac{1}{x^2}w_{xxx}$$
$$+ \frac{2}{3}A_2w_{xxy} + \frac{1}{3}A_2\frac{h_b^2}{h_a^2}(w_{yyyy}) - 4A_2\frac{h_a^2}{h_b}(u_xw_x)_{xx} - 2A_1\frac{h_a^3}{n_b^2}(u_xw_{xx})_{xx} + \frac{1}{6}A_4h_a(u_xw_{yy})_{xx}$$
$$- \frac{1}{6}A_3h_a(u_yw_{xy})_{xx} + \frac{1}{6}A_4h_a(u_xw_{xx})_{yy} + \frac{1}{6}A_4\frac{h_b^2}{h_a}(u_xw_{yy})_{yy} - \frac{1}{6}A_3\frac{h_b^2}{h_a}(u_yw_{xy})_{yy}$$
$$- 2A_2\frac{1}{h_a}(u_xw_y)_y - A_2\frac{1}{h_a}(u_yw_x)_y - A_2\frac{1}{h_a}(u_yw_y)_x - \frac{1}{3}A_3h_a(u_xw_{xy})_{xy}$$
$$- \frac{1}{6}A_3h_a(u_yw_{xx})_{xy} - \frac{1}{6}A_3\frac{h_b^2}{h_a}(u_yw_{yy})_{xy} - \frac{1}{6}A_3A_ah_b^2(v_xw_{xx})_{xy} - 4A_2\frac{h_b^2}{h_a}(v_yw_y)_y$$
$$- 2A_1\frac{h_b^3}{h_a}(v_yw_{yy})_{yy} + \frac{1}{6}A_4\frac{h_a^2}{h_b}(v_yw_{xx})_{xx} - \frac{1}{6}A_3h_a\frac{h_b^2}{h_b}(v_xw_{xy})_{xx} + \frac{1}{6}A_4h_b(v_yw_{yy})_{xx}$$
$$+ \frac{1}{6}A_4h_b(v_yw_{xx})_{yy} - \frac{1}{6}A_3h_b(v_xw_{xy})_{yy} - 2A_2\frac{1}{h_b}(v_yw_x)_x - A_2\frac{1}{h_b}(v_xw_x)_y$$
$$- A_2\frac{1}{h_b}(v_xw_y)_x - \frac{1}{3}A_3h_b(v_yw_{xy})_{xy} - \frac{1}{6}A_3h_b(v_xw_{yy})_{xy} - 2A_2\frac{h_a^2}{h_b^2}(w_x^3)_x$$
$$- 2A_2\frac{h_b^2}{h_a^2}(w_y^3)_y - A_2(w_xw_y^2)_x - A_2(w_x^2w_y)_y + A_1\frac{h_d^4}{h_b^2}(w_xw_{xx}^2)_x + A_1\frac{h_b^4}{h_a^2}(w_yw_{yy}^2)_y$$
$$- \frac{1}{12}A_4h_b(w_xw_{yy}^2)_x - \frac{1}{12}A_4h_a^2(w_{xx}^2w_y)_y - \frac{1}{6}A_4h_a(w_xw_{xx}w_{yy})_x$$
$$- \frac{1}{6}A_4h_b^2(w_{xx}w_yw_{yy})_y + \frac{1}{6}A_3h_a(w_xw_{xy}^2)_x + \frac{1}{6}A_3h_b(w_yw_{xy}^2)_y - A_1\frac{h_d^4}{h_b}(w_x^2w_{xx})_{xx}$$
$$- A_1\frac{h_b^4}{h_a^4}(w_y^2w_{yy})_{yy} + \frac{1}{12}A_4h_b^2(w_y^2w_{yy})_{xx} + \frac{1}{12}A_4h_a^2(w_x^2w_{xx})_{yy} + \frac{1}{12}A_4h_a^2(w_{xx}w_y^2)_{xx}$$

$$
\begin{aligned}
&+\frac{1}{12}A_4h_b\left(w_{xx}w_y^2\right)_{yy}+\frac{1}{12}A_4h_a\left(w_x^2w_{yy}\right)_{xx}+\frac{1}{12}A_4h_b\left(w_x^2w_{yy}\right)_{yy}\\
&-\frac{1}{6}A_3h_a\left(w_xw_yw_{xy}\right)_{xx}-\frac{1}{6}A_3h_b^2\left(w_xw_yw_{xy}\right)_{yy}-\frac{1}{6}A^3h_a^2\left(w_x^2w_{xy}\right)_{xy}\\
&-\frac{1}{6}A_3h_b^{\,2}\left(w_y^2w_{xy}\right)_{xy}-\frac{1}{6}A_3h_b^{\,2}\left(w_xw_yw_{yy}\right)_{xy}-\frac{1}{6}A_3h_a^{\,2}\left(w_xw_yw_{xx}\right)_{xy}-A_2\left(w_xw_y^2\right)_x\\
&-A_2\left(w_x^{\,2}w_y\right)_y+\frac{1}{6}A_3h_a^{\,2}\left(w_{xx}w_yw_{xy}\right)_x+\frac{1}{6}A_3h_a^{\,2}\left(w_xw_{xx}w_{xy}\right)_y+\frac{1}{6}A_3h_b\left(w_yw_{xy}w_{yy}\right)_x\\
&+\tfrac{1}{6}A_3h_b\left(w_xw_{xy}w_{yy}\right)_y+12A_1\frac{h_a^{\,2}}{h_b}\left(u_x^2w_x\right)_x-A_4\left(u_x^{\,2}w_y\right)_y+\frac{1}{2}A_3h_b^{\,2}\left(u_y^{\,2}w_y\right)_y\\
&+A_3\left(u_xu_yw_y\right)_x+A_3\left(u_xu_yw_x\right)_y+\frac{1}{2}A_3\left(u_y^2w_x\right)_x+12A_1h_b^{\,2}\left(v_y^{\,2}w_y\right)_y-A_4\left(v_y^2w_x\right)_x\\
&+\frac{1}{2}A_3\frac{h_a^{\,2}}{h_b^{\,2}}\left(v_x^2w_x\right)_x+A_3\left(v_xv_yw_y\right)_x+A_3\left(v_xv_yw_x\right)_y+\frac{1}{2}A_3\left(v_x^2w_y\right)_y-2A_4\frac{h_a}{h_b}\left(u_xv_yw_x\right)_x\\
&-2A_4\frac{h_b}{h_a}\left(u_xv_yw_y\right)_y+A_3\frac{h_a}{h_b}\left(u_yv_xw_x\right)_x+A_3\frac{h_b}{h_a}\left(u_yv_xw_y\right)_y+A_3\frac{h_a}{h_b}\left(u_xv_xw_y\right)_x\\
&-A_4h_b\left(v_yw_x^2w_y\right)_y+A_3h_b\left(v_xw_xw_y^2\right)_y-A_4h_b\left(v_yw_xw_y^2\right)_x-A_4\frac{h_a^{\,2}}{h_b}\left(v_yw_x^3\right)_x\\
&+A_3\frac{h_a^{\,2}}{h_b}\left(v_xw_x^2w_y\right)_x+A_3h_b\left(v_yw_x^2w_y\right)_y+\frac{1}{2}A_3h_b\left(v_xw_xw_y^2\right)_y+\frac{1}{2}A_3\frac{h_a^{\,2}}{h_b}\left(v_xw_x^3\right)_y\\
&+A_3h_b\left(v_yw_xw_y^2\right)_x+\frac{1}{2}A_3h_b\left(v_xw_y^3\right)_x+\frac{1}{2}A_3\frac{h_a^{\,2}}{h_b}\left(v_xw_x^2w_y\right)_x+3A_1\frac{h_a^{\,4}}{h_b}\left(w_x^5\right)_x \qquad (21)\\
&+3A_1h_b\left(w_y^5\right)_y-\frac{1}{4}A_4h_b^{\,2}\left(w_xw_y^4\right)_x-\frac{1}{4}A_4h_a\left(w_x^4w_y\right)_y-\frac{1}{4}A_sh_a^{\,2}\left(w_x^3w_y^2\right)_x\\
&-\frac{1}{4}A_sh_b^2\left(w_x^2w_y^3\right)_y+\frac{1}{2}A_3h_a^2\left(w_x^3w_y^2\right)_x+\frac{1}{2}A_3h_b^{\,2}\left(w_x^2w_y^3\right)_y+\frac{1}{2}A_3h_b^{\,2}\left(w_xw_y^4\right)_x\\
&+\frac{1}{2}A_3h_a^2\left(w_x^4w_y\right)_y=F\cos(\Omega t),
\end{aligned}
$$

$$
\begin{aligned}
&v_{tt} + M_{mass}\,d(x - x_{mass})\,d(y - y_{mass})\,v_{tt} - \frac{3}{h_a h_b}A_2 u_{xy} - \frac{4}{h_a^2}A_2 v_{yy} - \frac{1}{h_b^2}A_2 v_{xx} \\
&+\frac{1}{2}\frac{h_b}{h_a}A_3\left(u_y^2\right)_y + \frac{1}{h_b}A_3\left(u_x u_y\right)_x - \frac{2}{h_a}A_4\left(u_x v_y\right)_y + \frac{1}{h_a}A_3\left(u_y v_x\right)_y \\
&+\frac{1}{h_b}A_3\left(v_y v_x\right)_x - 2\frac{h_b}{h_a}A_2\left(w_y^2\right) - \frac{A_2}{h_b}\left(w_x^2\right)_y + \frac{h_b^3}{h_a}A_1\left(w_{yy}{}^2\right)_y - \frac{2A_4}{h_b}u_x u_{yx} \\
&-\frac{1}{12}\frac{h_a^2}{h_b}A_4\left(w_{xx}{}^2\right)_y - \frac{1}{6}h_b A_4\left(w_{xx}w_{yy}\right)_y + \frac{1}{6}h_b A_3\left(w_{xy}{}^2\right)_y - \frac{1}{h_b}A_2\left(w_x w_y\right)_x \\
&+\frac{1}{6}\frac{1}{h_b^2}A_3\left(w_{xx}w_{xx}\right)_x + \frac{1}{6}h_b A_3\left(w_{xy}w_{yy}\right)_x - \frac{h_a}{h_b}A_A\left(u_x w_x^2\right)_y - \frac{h_b}{h_a}A_A\left(u_x w_y^2\right)_y \\
&+\frac{h_b}{h_a}A_3\left(u_y w_x w_y\right)_y + \frac{h_a}{h_b}A_3\left(u_x w_x w_y\right)_x + \frac{1}{2}\frac{h_a}{h_b}A_3\left(u_y w_x^2\right)_x + \frac{1}{2}\frac{1}{h_b}h_a A_3\left(u_y w_y^2\right)_x \\
&+12\frac{h_b^2}{h_a^2}A_1\left(v_y w_y^2\right)_y - A_4\left(v_y w_x^2\right)_y + A_3\left(v_x w_x w_y\right)_y + \frac{1}{2}\frac{1}{h_b^2}A_3\left(v_x w_x^2\right)_x \\
&+\frac{1}{2}A_3\left(v_x w_y^2\right)_x + A_3\left(v_y w_x w_y\right)_x + 3\frac{h_b^3}{h_a^3}A_1\left(w_y^4\right)_y - \frac{1}{4}h_a^2 A_4\left(w_x^4\right)_y \\
&-\frac{1}{4}h_b A_4\left(w_x^2 w_y^2\right)_y + \frac{1}{2}\frac{h_a^2}{h_b}A_3\left(w_x^3 w_y\right)_x + \frac{1}{2}h_b A_3\left(w_x w_y^3\right)_x = 0
\end{aligned}
\tag{22}
$$

3.3 Solution Methodology

The Galerkin method was adopted because of its computational simplicity and accuracy, as further confirmed by the good agreement between the present results and the reference data [58, 59]. For the rectangular plate considered in this study, fully clamped edges are assumed, and the corresponding geometric boundary conditions are:

$$u = v = w = 0, \quad \frac{\partial w}{\partial x} = 0, \quad x = 0,1 \tag{23a}$$

$$u = v = w = 0, \quad \frac{\partial w}{\partial y} = 0, \quad y = 0,1 \tag{23b}$$

It should be noted that the admissible functions and Galerkin coefficients used in the present formulation are constructed for the fully clamped boundary condition. Other boundary conditions would require different admissible functions and recalculation of the corresponding modal mass, stiffness, and nonlinear coefficients. Therefore, the present results should be

interpreted specifically for fully clamped GPL-reinforced hyperelastic plates. In the Galerkin method, the displacements are written as modal expansions:

$$u(x,y,t)=\sum_{i=1}^{M}\sum_{j=1}^{M}U_{ij}(t)f_i(x)y_j(y) \quad (24a)$$

$$v(x,y,t)=\sum_{i=1}^{M}\sum_{j=1}^{M}V_{ij}(t)f_i(x)y_j(y) \quad (24b)$$

$$w(x,y,t)=\sum_{i=1}^{M}\sum_{j=1}^{M}W_{ij}(t)X_i(x)Y_j(y) \quad (24c)$$

For the in-plane displacements u and v, only the zero-displacement condition at the plate boundaries must be satisfied. For the transverse displacement w, the clamped-mode shape function is employed to satisfy both the zero deflection and zero slope boundary conditions. Consequently:

$$f_i(x)=\sin(i\pi x), \quad (25)$$

$$y_j(y)=\sin(j\pi y), \quad (26)$$

$$X_i(x)=\cosh(\beta_i x)-\cos(\beta_i x)-\frac{\cosh(\beta_i)-\cos(\beta_i)}{\sinh(\beta_i)-\sin(\beta_i)}\left[\sinh(\beta_i x)-\sin(\beta_i x)\right], \quad (27)$$

$$Y_j(y)=\cosh(\beta_j y)-\cos(\beta_j y)-\frac{\cosh(\beta_j)-\cos(\beta_j)}{\sinh(\beta_j)-\sin(\beta_j)}\left[\sinh(\beta_j y)-\sin(\beta_j y)\right] \quad (28)$$

After substituting the series expansions (25)–(28) into the non-dimensional governing equations (20)–(22) and applying the Galerkin method, the nonlinear partial differential equations are reduced to a set of nonlinear ordinary differential equations. These can be written in the following compact matrix form:

$$\mathbf{M}\ddot{\mathbf{X}}+\mathbf{C}\dot{\mathbf{X}}+\mathbf{K}_L\mathbf{X}+\mathbf{K}_{NL}(\mathbf{X})\mathbf{X}=\mathbf{F}(t) \quad (29)$$

where $\mathbf{X}=[\mathbf{U}\ \mathbf{V}\ \mathbf{W}]^{\mathrm{T}}$ is the vector of unknown time-dependent generalized coordinates, with $\mathbf{U}=[U_{11},U_{12},\ldots,U_{NN}]^T$, $\mathbf{V}=[V_{11},V_{12},\ldots,V_{NN}]^T$, $\mathbf{W}=[W_{11},W_{12},\ldots,W_{NN}]^T$. $\mathbf{M}$ is the mass matrix, including the effect of a concentrated mass if present. The damping term $\mathbf{C}\dot{\mathbf{X}}$ is introduced as a phenomenological linear viscous damping term. In the reduced one-term

transverse equation used in the present simulations, this damping contribution appears as $cW\dot{}$, where c is a constant modal viscous damping coefficient [60, 61]. This damping term represents lumped structural energy dissipation and is not treated as a nonlinear, viscoelastic, frequency-dependent, amplitude-dependent, temperature-dependent, or GPL-content-dependent quantity in the present study. $\mathbf{K}_{\mathrm{L}}$ is the linear stiffness matrix. $\mathbf{K}_{NL}(\mathbf{X})$ is the nonlinear stiffness matrix, which depends on the solution $\mathbf{X}$, and $\mathbf{F}(t)$ is the external force vector.

In the reduced equations, damping is retained only as a linear viscous modal damping term in the transverse generalized coordinate, represented by $cW\dot{}$. By retaining only one term in the Galerkin series expansions, the discretized equations of motion are reduced to the following set of nonlinear ordinary differential equations:

$$M_{11}\ddot{U}+K_{L11}U+K_{L12}V+K_{NL11}U^2+K_{NL12}UV +K_{NL13}V^2+K_{NL14}W^2+K_{NL15}UW^2+K_{NL16}VW^2+K_{NL17}W^4=0, \tag{30}$$

$$M_{22}\ddot{V}+K_{L21}U+K_{L22}V+K_{NL21}U^2+K_{NL22}UV +K_{NL23}V^2+K_{NL24}W^2+K_{NL25}UW^2+K_{NL26}VW^2+K_{NL27}W^4=0, \tag{31}$$

$$M_{33}\ddot{W}+c\dot{W}+K_{L33}W+K_{NL31}UW+K_{NL32}VW+K_{NL33}U^2W +K_{NL34}UVW+K_{NL35}V^2W+K_{NL36}W^3+K_{NL37}UW^3+K_{NL38}VW^3+K_{NL39}W^5=f_0\cos(\Omega t), \tag{32}$$

3.4 Numerical Solution and Analysis

To solve the set of nonlinear ordinary differential equations resulting from the Galerkin discretization, the well-established fourth-order Runge–Kutta method is employed. This explicit time-integration scheme is widely used for nonlinear dynamic systems due to its high accuracy, numerical stability, and ease of implementation. Unlike implicit methods, the Runge–Kutta method does not require the solution of a system of nonlinear algebraic equations at each time step, making it particularly efficient for obtaining time-history responses, phase-plane trajectories, and Poincaré maps. Furthermore, its fourth-order accuracy ensures reliable capturing of the nonlinear characteristics—such as hardening/softening behavior and

frequency shifts—without introducing excessive numerical damping. A convergence study was performed to select an appropriate time step, ensuring that the results are independent of the step size.

The frequency–response curves and bifurcation characteristics of the reduced nonlinear dynamical system were computed using the numerical continuation and bifurcation analysis package AUTO [62]. Periodic solutions were obtained using a pseudo–arclength continuation scheme, which allows both stable and unstable solution branches to be followed through turning points and bifurcations. In AUTO, periodic orbits were discretized using orthogonal collocation on finite elements with adaptive mesh refinement. In the present simulations, each periodic solution was represented using NTST=50 mesh intervals with NCOL=4 collocation points per interval, which was verified to provide mesh-independent results.

The continuation process was initiated from a small-amplitude periodic solution near the primary resonance obtained from time-domain simulations. The step size was adaptively controlled with an initial continuation step (DS=10^{-3}), maximum step size (DSMAX=10^{-4}), and minimum step size (DSMIN=10^{-6}). The convergence tolerances for the Newton iterations were specified as (EPSL=10^{-3}) and (EPSU=10^{-8}), while the residual tolerance was set to (EPS=10^{-7}).

During continuation, the excitation frequency was treated as the principal continuation parameter. The stability of the computed periodic solutions was determined by evaluating the corresponding Floquet multipliers automatically provided by AUTO, enabling a clear identification of stable and unstable branches of the frequency–response curves as well as the detection of bifurcation points such as saddle–node and period-doubling bifurcations. Additional mesh refinement tests were also conducted to ensure that the obtained solutions were independent of the discretization parameters.

4. Results and Discussion

Motivated by the need to understand how GPL-induced material nonlinearity influences the dynamic performance of compliant polymer plates, this section first presents the experimentally determined mechanical properties and Mooney–Rivlin constants of the GPL–epoxy nanocomposites. The subsequent vibration analyses are then organized to clarify the scientific mechanisms governing resonance shift, amplitude variation, mass sensitivity, and the transition between softening- and hardening-type nonlinear responses.

4.1 Hyperelastic Material Constants

Tensile tests were performed on nanocomposite specimens reinforced with six different GPL weight fractions: 0, 0.2, 0.4, 0.6, 0.8, and 1 wt.%. The resulting tensile stress–strain curves for the nanocomposites with different GPL weight fractions are shown in Figure 5a. As observed, the elastic modulus of the nanocomposite increases with increasing GPLs weight fraction. Furthermore, the yield strength and ultimate tensile strength of the nanocomposites also exhibit an increasing trend with increasing weight fraction up to 0.8 wt.%, after which they decrease. Because the addition of GPLs causes the matrix behavior to become more brittle, the fracture strain of the nanocomposite specimens is expected to decrease with increasing GPLs weight fraction, and this downward trend in fracture strain is clearly observed in Figure 5a. Figure 5a shows that the sample containing 0.8 wt.% GPLs has the highest ultimate tensile strength. When the GPL concentration is increased to 1.0 wt.%, the nanocomposite remains stronger than pure epoxy; however, its ultimate tensile strength and fracture strain decrease. This trend is attributed to GPL agglomeration at higher weight fractions, which produces local stress concentration zones, reduces effective load transfer, promotes premature damage initiation, and consequently lowers the structural reliability of the nanocomposite. Therefore, 0.8 wt.% GPLs can be regarded as the optimum concentration from the tensile-strength viewpoint, because it provides the highest ultimate tensile strength; however, this

mechanical optimum should be distinguished from the vibration-performance optimum, which is mainly governed by effective stiffness. While lower weight fractions (0.2% to 0.6%) result in a gradual increase in strength compared to pure epoxy, a reduction in fracture strain and ultimate tensile stress is observed at higher weight fractions (1.0 wt.%). Figure 5b shows images of the standard tensile test specimens after performing the corresponding test. Based on the fracture morphology of the tensile specimens, the samples exhibit brittle-type fracture, which is consistent with their stress–strain response.

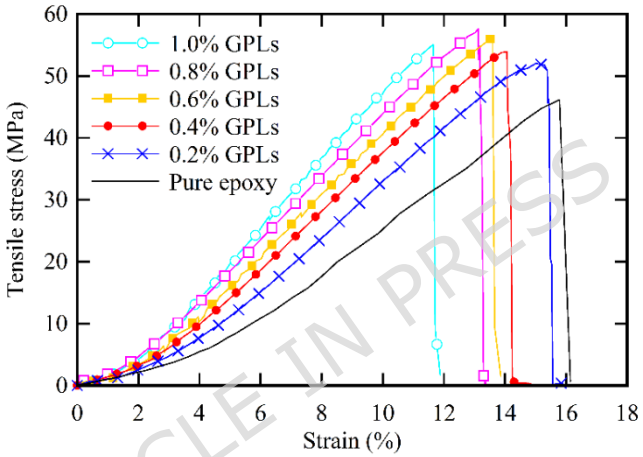

(a)

(b)

Figure 5: (a) Tensile stress-strain curves of epoxy nanocomposite reinforced with GPLs, (b) standard tensile test specimens of nanocomposite after direct tensile testing.

Figure 6 shows microscopic images of the fracture surface of the GPLs-reinforced nanocomposite. The SEM images indicate that, at suitable GPL contents, the graphene layers are effectively separated and dispersed within the epoxy matrix. At 0.8 wt.% GPLs, the graphene layers appear more effectively separated and distributed within the epoxy matrix, which improves interfacial load transfer; however, at 1.0 wt.% GPLs, agglomerated regions are observed, and these clusters act as stress concentration sites that reduce reinforcement efficiency, tensile strength, and fracture strain. The SEM observations provide microstructural support for the mechanical trends obtained from the tensile tests. At 0.8 wt.% GPLs, the graphene layers are more effectively separated and distributed within the epoxy matrix, which promotes interfacial load transfer and improves the reinforcing efficiency of the nanoplatelets. However, when the GPL content is increased to 1.0 wt.%, agglomerated regions become more evident. These agglomerates behave as local defects and stress concentration sites, reducing the efficiency of stress transfer from the matrix to the nanoplatelets and contributing to the observed reduction in ultimate tensile strength and fracture strain. This microstructural evidence confirms that the mechanical properties of GPL-reinforced nanocomposites are governed not only by the filler content, but also by the quality of nanoparticle dispersion.

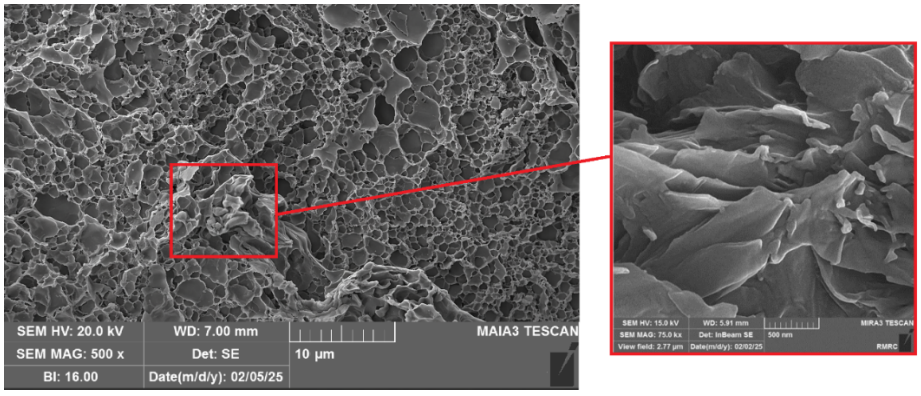

(a)

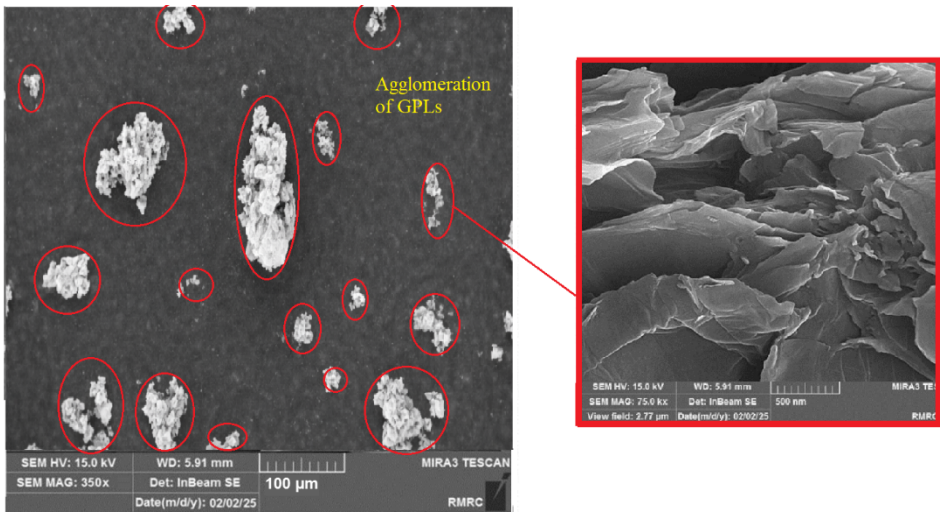

(b)

Figure 6: Microscopic images of the fracture surface of the reinforced nanocomposite sample: (a) 0.8 wt.% GPLs, and (b) 1 wt.% GPLs. Agglomerated regions are marked with red circles and arrows for clarity.

In this study, the Mooney–Rivlin hyperelastic model coefficients were extracted to characterize the nonlinear mechanical behavior of epoxy nanocomposites reinforced with GPLs. Direct tensile tests were performed on pure epoxy and GPL-reinforced epoxy specimens with different GPL weight fractions. The experimentally measured stress–strain curves were used as the input data for identifying the Mooney–Rivlin constants C_1 and C_2. For each GPL concentration, the experimental strain data were first converted into the stretch ratio $\lambda=1+\varepsilon$, and the corresponding stress response was fitted to the uniaxial Mooney–Rivlin stress relation using a nonlinear least-squares procedure. This fitting minimized the difference between the measured tensile stress and the stress predicted by the hyperelastic model over the experimental strain range. The calibrated constants were then directly used in the strain-energy density function of the plate and consequently in the nonlinear vibration equations. Therefore, tensile testing contributes to accurate modelling by ensuring that the material parameters used in the vibration analysis reflect the actual

nonlinear stress–strain response of the fabricated GPL–epoxy nanocomposites, rather than assumed or idealized material properties. The material constants C_1 and C_2 were obtained by minimizing the following least-squares error function:

$$\min_{C_1,C_2} \sum_{k=1}^{N} \left[\sigma_{\exp}(I_k) - \sigma_{MR}(I_k; C_1, C_2) \right]^2 \quad (33)$$

where σ_{exp} is the experimentally measured tensile stress and σ_{MR} is the stress predicted by the Mooney–Rivlin model. The optimized constants were then directly introduced into the strain-energy density function of the plate. In this way, the vibration model incorporates the real nonlinear material behaviour of the GPL–epoxy nanocomposite, including the influence of GPL dispersion, stiffness enhancement, and possible agglomeration at higher filler contents. This experimentally calibrated procedure is more accurate than using assumed hyperelastic constants or equivalent linear elastic properties, because it transfers the measured material response directly into the nonlinear governing equations.

Figure 7 compares the experimental stress–strain data of the nanocomposite containing 0.2 wt.% GPLs with the predictions of three commonly used hyperelastic models: Neo-Hookean, Mooney–Rivlin, and Ogden. The experimental curve shows a clear nonlinear response with gradual strain stiffening, which is characteristic of particle-reinforced polymer nanocomposites. Among the three models, the Mooney–Rivlin formulation provides the closest overall agreement with the experimental stress–strain data over the investigated strain range. This improved agreement is attributed to its two-parameter structure, in which C_1 represents the initial stiffness contribution and C_2 accounts for the shear-sensitive nonlinear contribution associated with the second strain invariant. The Neo-Hookean model gives acceptable predictions only at small strains, but it progressively underestimates the stress at higher strains because its one-parameter form cannot adequately capture strain-induced stiffening. The Ogden model is more flexible; however, for the available uniaxial tensile

dataset, its additional parameters do not provide a clear improvement over the Mooney–Rivlin model and may increase the risk of non-unique parameter identification. Therefore, the Mooney–Rivlin model was selected because it provides the best compromise between experimental fitting accuracy, physical interpretability, robust parameter identification, and computational tractability. The experimentally identified Mooney–Rivlin coefficients, C_1 and C_2, are listed in Table 1 and were subsequently used in the strain-energy density function and nonlinear vibration analysis of the GPL-reinforced polymer plate.

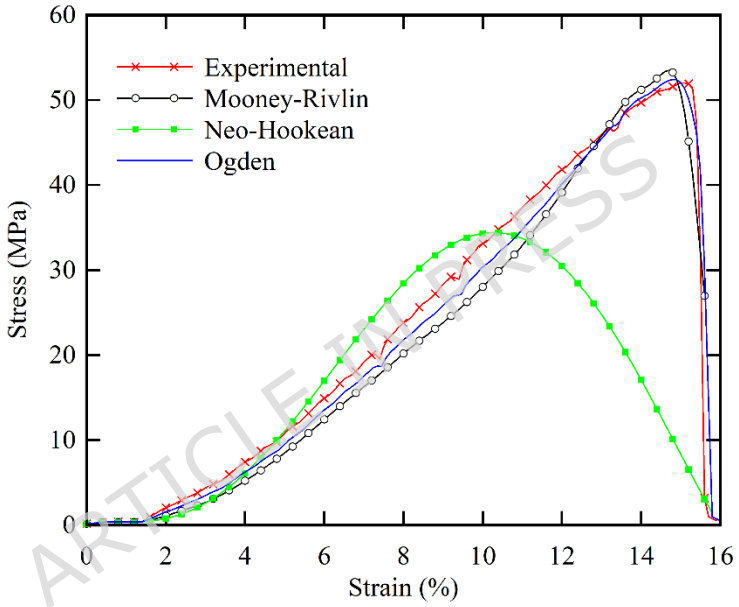

Figure 7: Comparison of experimental stress–strain data for the nanocomposite containing 0.2 wt.% GPLs with predictions from the Neo-Hookean, Mooney–Rivlin, and Ogden hyperelastic models.

Table 1: Mooney-Rivlin model coefficients for epoxy reinforced with GPLs.

Material	Coefficient	
	C_1 (GPa)	C_2 (GPa)
Pure epoxy	3.5115	-3.3825
Epoxy+0.2 wt.% GPLs	4.8243	-4.6783

Epoxy+0.4 wt.% GPLs	5.3990	-5.1973
Epoxy+0.6 wt.% GPLs	6.7296	-6.5715
Epoxy+0.8 wt.% GPLs	7.8675	-7.5567
Epoxy+1.0 wt.% GPLs	8.6457	-8.4619

4.2 Vibration Analysis

The nonlinear dynamic response of GPL-R hyperelastic plates is examined in this section. Nonlinear analysis is essential for comprehending the mechanical response of polymeric nanocomposite hyperelastic structures under a variety of circumstances because these structures' nonlinear mechanical properties are exacerbated by the high strains brought on by their soft behavior. Validating the approach and solution process used is the first step in this section. The significance of taking coupled motion into account and the impact of different parameters on the nonlinear response are then examined.

To investigate the dynamic behavior of the structure, the following properties are considered: a= 200 mm, h = 10 mm, b = 100 mm, ρ = 1150 kg/m ^{3}, F_0 = 50 N. The hyperelastic properties for the different nanocomposites are taken from Table 1. The concentrated mass M_{mass} is attached at the point (x_{mass}, y_{mass})=(0.5, 0.5), i.e., the geometric center of the plate. The harmonic concentrated force $F(t)$ is applied at the same location (x_{force}, y_{force})=(0.5, 0.5) to excite the fundamental mode symmetrically. These positions remain fixed throughout all numerical simulations presented in this study.

4.2.1 Validation and Convergence

To validate the current procedure, two distinct methods are employed. First, the constants are selected to match the mechanical and physical

properties used in reference [63]. In that reference, the vibrational behavior was studied using Mooney–Rivlin hyperelastic constants of C_1 = 25.829 kPa and C_2 = 649.612 MPa. Considering the first two terms of the assumed solution series and the first two Galerkin terms (M = 2), the frequency-response curve of the structure is obtained, as shown in Figure 8. As can be seen, the results demonstrate excellent agreement with reference [63], validating the accuracy of present approach.

Furthermore, the convergence of the current methodology is analyzed by increasing the total number of modes (the number of terms in the Galerkin method). For this purpose, the hyperelastic nanocomposite plate is modeled using the properties given at the beginning of this section for the 0.6 wt.% GPL-containing nanocomposite and F=0.1F_0. As shown in Figure 9, by increasing the number of modes from 5 to 15, convergence is achieved after considering ten modes, and this number of modes will be used in this study.

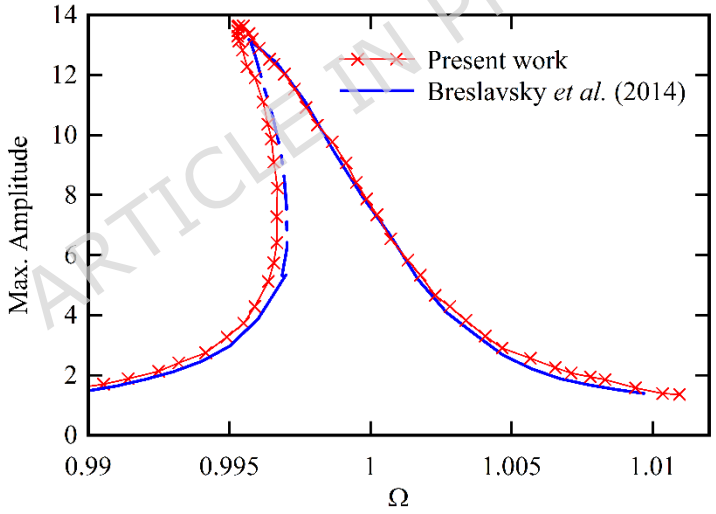

Figure 8: Comparison of the frequency-response curve for an isotropic hyperelastic plate with results from the literature.

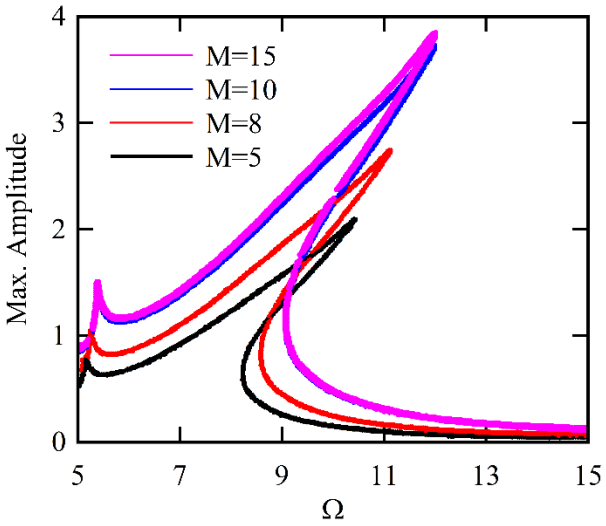

Figure 9: Effect of the number of Galerkin terms on the convergence of the nonlinear frequency response of the 0.6 wt.% GPL-containing nanocomposite plate.

4.2.2 Effect of Hyperelastic Constitutive Assumption

Linear elastic models are insufficient for the present GPL-reinforced polymer plates because they assume a constant stiffness and a proportional stress–strain relation, whereas the experimentally observed response of the nanocomposite is nonlinear and its tangent stiffness evolves with strain. In other words, the relationship between stress and strain is nonlinear, which diminishes the precision of linear models in predicting mechanical behavior due to their simplified assumptions. This section examines results obtained using both elastic and hyperelastic plate theories. To enable comparison, an equivalent Young's modulus is used for the elastic plate theory. The effective Young's modulus of the nanocomposite is obtained from the strain energy as follows:

$$E_{eff} = \left. \frac{\partial^2 W}{\partial e^2} \right|_{e=e_{avg}} \quad (40)$$

Figure 10 compares the time-domain response of free and forced vibrations of a nanocomposite plate with 0.2 wt.% GPLs for both elastic and hyperelastic models, with M_{mass}=0.1 and F_o = 0.2. The maximum oscillation

amplitude obtained from the elastic model is 1.19, while the hyperelastic model yields 0.92. The hyperelastic model predicts a maximum oscillation amplitude that is 22.7% lower. This reduction indicates that the deformation-dependent tangent stiffness captured by the hyperelastic formulation modifies the nonlinear restoring force and reduces the predicted large-amplitude dynamic response compared with the constant-stiffness linear elastic approximation. The discrepancy between the linear elastic and hyperelastic predictions becomes more pronounced as the vibration amplitude increases. This is because the linear elastic model uses a constant equivalent Young's modulus and therefore represents only a local small-strain approximation of the actual material response. It cannot update the tangent stiffness as deformation evolves and cannot account for the nonlinear strain-energy contributions associated with the Mooney–Rivlin invariants. As a result, it neglects the material part of the nonlinear restoring force and retains only the simplified elastic stiffness contribution. The hyperelastic model, on the other hand, captures the deformation-dependent stiffness of the GPL-reinforced polymer and its coupling with geometric nonlinearity caused by membrane stretching. For the 0.2 wt.% GPL-reinforced plate considered in Fig. 10, the maximum vibration amplitude predicted by the linear elastic model is 1.19, whereas the hyperelastic model predicts 0.92, corresponding to a 22.7% reduction. This difference demonstrates that the linear elastic model overestimates the large-amplitude response and may lead to inaccurate predictions of resonance amplitude, frequency shift, and nonlinear stability characteristics. These results demonstrate that a full hyperelastic constitutive description is necessary for accurately predicting large-amplitude vibrations of GPL-reinforced polymer plates, particularly when resonance amplitude, frequency shift, jump phenomena, and softening-to-hardening transitions are of interest.

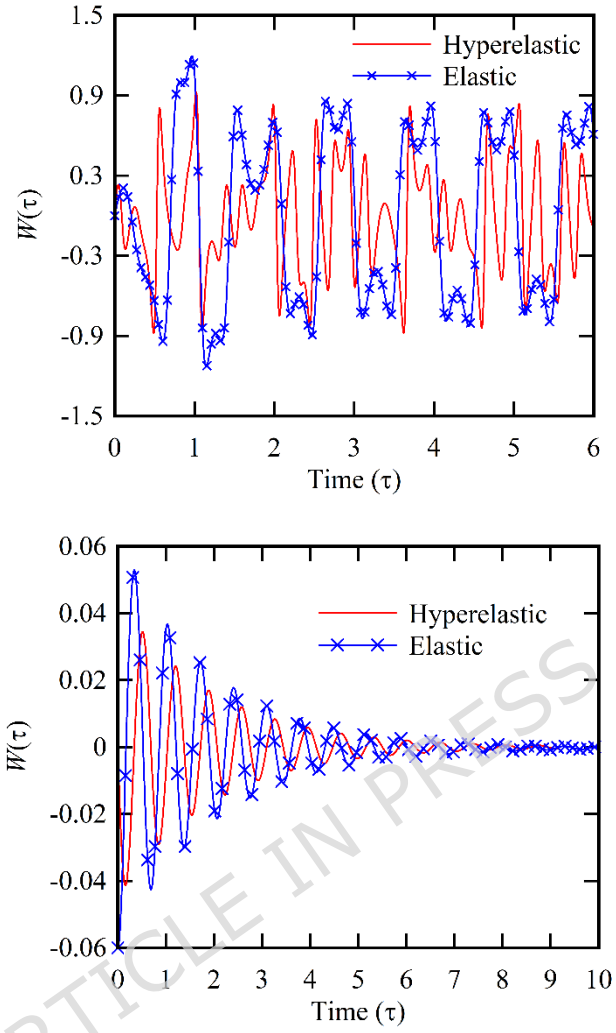

(a) (b)

Figure 10: Time-domain response of (a) free and (b) forced vibrations of a nanocomposite plate containing 0.2 wt.% GPLs for M_{mass}=0.1 and F_o = 0.2, comparing elastic and hyperelastic models.

From a design perspective, the use of a linear elastic model may introduce significant errors in predicting the vibration behavior of GPL-reinforced polymer plates. For the case shown in Fig. 10, corresponding to the 0.2 wt.% GPL-reinforced plate with M_{mass}=0.1 and F_0=0.2, the maximum vibration amplitude predicted by the linear elastic model is 1.19, whereas the hyperelastic model predicts 0.92. Thus, if the hyperelastic prediction is considered as the more representative response because it incorporates the

experimentally calibrated nonlinear material behavior, the linear model overestimates the maximum amplitude by approximately 29.3%. Equivalently, the hyperelastic prediction is 22.7% lower than the linear elastic prediction when the linear result is used as the reference. This discrepancy arises because the linear model employs a constant equivalent Young's modulus and cannot update the tangent stiffness as the deformation amplitude increases. Therefore, the error is expected to become more pronounced under large-amplitude vibration. In addition to amplitude overprediction, the linear model may also misrepresent the resonance location, frequency-response curvature, jump phenomena, and stability characteristics because it cannot capture the competing effects of Mooney–Rivlin material nonlinearity and von Kármán geometric nonlinearity. Hence, using a linear model in design may lead to inaccurate estimation of vibration levels, inappropriate selection of GPL content, and unreliable prediction of nonlinear resonance and stability margins.

A summary of the possible design errors is provided in Table 2. Table 2 shows that the most direct error caused by using a linear elastic model is the overestimation of the maximum vibration amplitude. In the studied case, the error reaches 29.3% when the hyperelastic result is used as the reference. However, the design error is broader than this single numerical difference. The linear model replaces the actual nonlinear material response with a constant equivalent stiffness and therefore cannot represent the evolution of tangent stiffness with deformation. As a result, it may predict an incorrect resonance location and cannot properly reproduce the curvature of the nonlinear frequency-response curve.

Table 2: Possible design errors caused by using a linear elastic model instead of the hyperelastic model.

Predicted quantity	Possible error when using a linear model	Justification
Maximum vibration amplitude	Overestimation of amplitude; 29.3% error for the 0.2 wt.% GPL case studied in Fig. 10	The linear model assumes constant stiffness, while the hyperelastic

Predicted quantity	Possible error when using a linear model	Justification
		model captures deformation-dependent tangent stiffness
Resonance frequency	Incorrect prediction of resonance location	Linear stiffness does not vary with vibration amplitude
Frequency-response curve	Failure to capture nonlinear curvature of the response branch	Mooney–Rivlin material nonlinearity and von Kármán geometric nonlinearity are not simultaneously represented
Jump and multi-stability regions	Possible omission or inaccurate prediction	The linear model cannot reproduce nonlinear branch bending and stability changes
Softening-to-hardening transition	Misclassification of nonlinear response regime	The transition depends on the competition between material-induced softening and geometry-induced hardening
GPL-content design	Inaccurate selection of reinforcement level	The influence of GPL concentration on C_1, C_2, resonance shift, and amplitude reduction is not captured by a purely linear model

4.2.3 Mass Sensitivity Analysis

In this subsection, the mass sensitivity of the hyperelastic nanocomposite plate is analyzed using hyperelastic plate theory. The added mass is small compared to the overall dimensions of the hyperelastic nanocomposite plate. Figure 11 illustrates the nonlinear behavior of hyperelastic nanocomposite for various values of M_{mass}. As observed, increasing the concentrated mass shifts the maximum vibration amplitude to lower frequencies and makes the nonlinear hardening behavior more pronounced. The results indicate that, in the absence of a concentrated mass, the system exhibits softening behavior, and the natural frequency decreases with increasing vibration amplitude. With the addition of a concentrated mass, the frequency corresponding to the maximum vibration amplitude shifts to lower values. In addition, as the concentrated mass increases, the nonlinear behavior of the system in the hardening region becomes more pronounced. Specifically, the numerical data show that, in the absence of a concentrated mass, the maximum vibration amplitude is 0.12, while with the

addition of a concentrated mass M_{mass}=0.2, this value increases to 0.23, representing an increase of approximately 95% in the maximum oscillation amplitude of the system. This 95% increase in amplitude reflects the significant role of the concentrated mass in altering the dynamic response of the system. From a physical point of view, the addition of a concentrated mass leads to an increase in the inertial force and increases the energy stored in the system, which results in an increase in the amplitude of oscillations and a change in the nonlinear behavior of the structure. These changes have a direct impact on the design and performance of dynamic systems affected by nonlinear loads.

The frequency–amplitude curves in Fig. 11 reveal two key nonlinear phenomena that deserve physical explanation. First, the system exhibits a transition from softening to hardening behavior as the concentrated mass increases. This stiffness evolution originates from the competition between two nonlinear mechanisms: geometric nonlinearity induced by large deflections (which typically produces hardening due to membrane stretching) and material nonlinearity inherent to the hyperelastic constitutive law (which can introduce softening depending on the strain energy function). In the absence of a concentrated mass, the material nonlinearity dominates at moderate amplitudes, leading to a softening response—i.e., a decrease in the effective natural frequency with increasing vibration amplitude. As the concentrated mass increases, the inertial forces amplify the membrane stretching effect, gradually shifting the balance toward a hardening regime where the frequency increases with amplitude.

Second, the initial softening observed for the clamped plate—even without an added mass—can be attributed to the specific form of the Mooney–Rivlin strain energy function employed. For this material model, the second invariant I_2 contributes terms that can reduce the effective stiffness under certain deformation patterns, particularly those involving significant shear or twist near the clamped boundaries. At low to moderate amplitudes, these boundary-layer effects dominate the response, producing a net softening.

Only when the amplitude becomes sufficiently large—or when an added mass enhances the membrane action—does the geometric hardening prevail. This interplay between material-induced softening and geometry-induced hardening is a characteristic feature of hyperelastic plates and underscores the importance of using a full nonlinear constitutive model rather than an equivalent linear approximation.

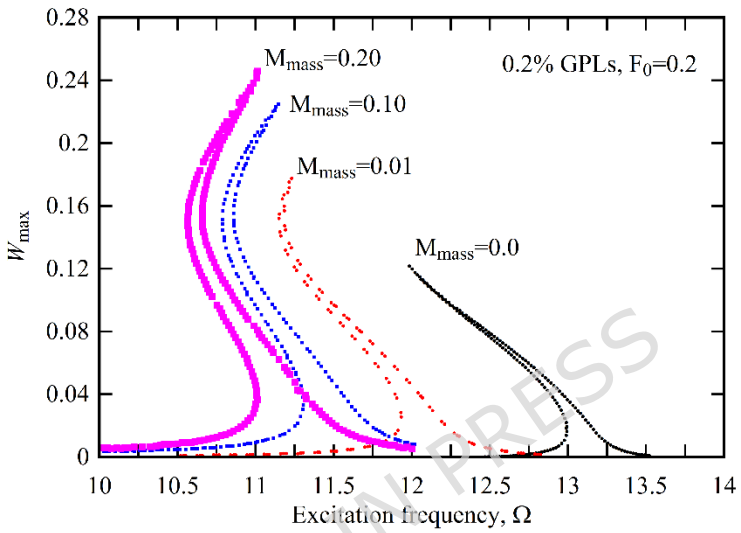

Figure 11: Nonlinear frequency response function illustrating the mass sensitivity of the hyperelastic plate for various values of M_{mass}.

It should be noted that all results presented herein correspond to the concentrated mass placed at the plate center. The mass location is known to affect modal participation factors and may alter the observed nonlinear behavior, particularly the softening-to-hardening transition. A systematic investigation of mass position effects, while beyond the scope of the present study, represents a valuable direction for future work.

4.2.4 Influence of Hyperelastic Material Parameters

The Mooney–Rivlin hyperelastic model, with stiffness coefficients C_1 and C_2 is used to define the strain-energy density of the nanocomposite plate. This section will examine the impact of the Mooney-Rivlin coefficients on the nonlinear response of the nanocomposite plate reinforced with 0.2 wt.% GPLs

in order to illustrate the significance of appropriately defining the values of these coefficients.

Figure 12 illustrates the effect of the Mooney–Rivlin parameters C_1 and C_2 on the nonlinear frequency-response of the nanocomposite plate containing 0.2 wt.% GPLs. As shown in Figure 12(a), increasing C_1 enhances the distortion of the frequency-response curve, shifting the system toward a more pronounced hardening behavior. Physically, C_1 is associated with the initial shear modulus and governs the material's resistance to deformation at moderate strains. An increase in C_1 elevates the effective stiffness of the material, which amplifies the geometric nonlinearity arising from membrane stretching and leads to a more prominent hardening response. Concurrently, the maximum oscillation amplitude decreases, as a stiffer material undergoes smaller deformations under the same external excitation. The peak of the frequency-response also shifts to higher frequencies, reflecting the increase in natural frequency due to the enhanced stiffness.

Figure 12(b) depicts the influence of the second parameter C_2. Unlike C_1, which dominates the response at small to moderate strains, C_2 is primarily sensitive to shear deformations and becomes more influential in regions with high strain gradients—such as near the clamped boundaries or in the vicinity of the concentrated mass. Increasing C_2 intensifies the contribution of the second invariant I_2 to the strain-energy density, which can locally reduce the effective stiffness under certain deformation patterns. This results in a more complex nonlinear response, where the softening effects near the boundaries compete with the global hardening induced by membrane action. For the material investigated in this study, the value of C_2 is significantly larger than C_1, making its influence on the overall dynamic behavior particularly pronounced. This explains the observed sensitivity of the frequency-response curves to variations in C_2, as well as the enhanced nonlinear distortion compared to materials with lower C_2 values.

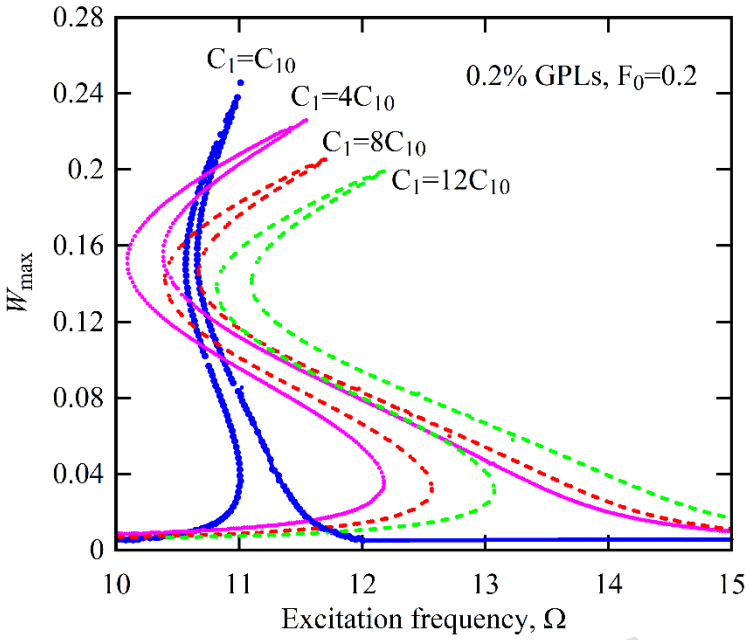

(a)

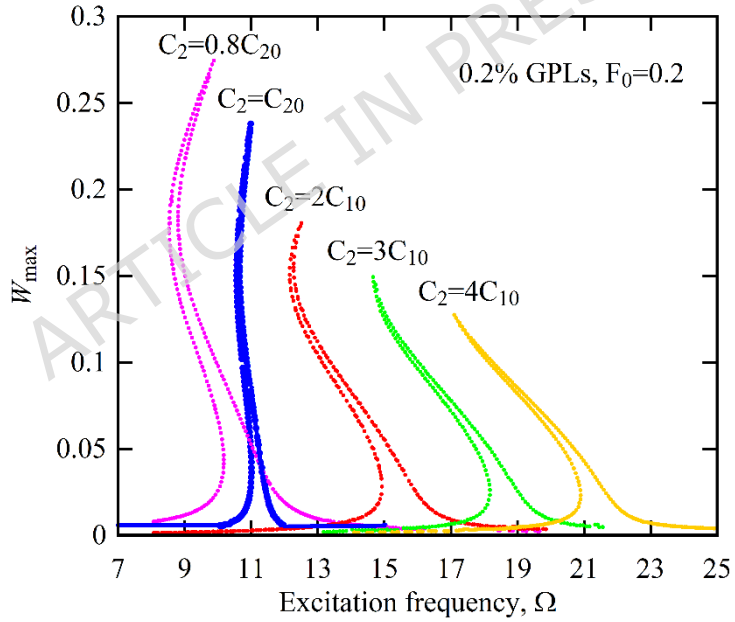

(b)

Figure 12: (a) Effect of the first Mooney-Rivlin model constant (C_1) and (b) effect of the second Mooney-Rivlin model constant (C_2) on the nonlinear frequency-response curve of the nanocomposite plate with 0.2 wt.% GPLs.

The sensitivity of the nonlinear frequency response to variations in C_1 and C_2 was quantified by computing the percentage change in resonant frequency and peak amplitude for ±20% variations in each parameter. A 20% increase in C_1 results in an approximate 8% increase in resonant frequency and a 12% reduction in peak amplitude. The same relative increase in C_2 produces a more modest 3% frequency shift but a 15% change in the curvature of the frequency-response curve, reflecting its role in shaping nonlinear distortion rather than linear stiffness. The observed sensitivity of vibration characteristics to C_1 and C_2 provides practical design insights. For applications requiring high resonant frequencies and low vibration amplitudes (e.g., precision instruments), formulations with higher C_1 are desirable. Conversely, if controlled nonlinearity or energy dissipation is sought (e.g., vibration isolators), tailoring C_2 through GPL concentration and dispersion offers a tuning mechanism. The experimentally established relationship between GPL content and Mooney–Rivlin constants thus enables the rational design of nanocomposite plates with targeted dynamic performance.

4.2.5 Effect of GPL-reinforcement

This section investigates the effect of GPL reinforcement on the nonlinear vibrational behavior of the nanocomposite plate. The presence of GPLs in the polymer matrix leads to a change in the mechanical properties, particularly an increase in the effective Young's modulus and improved material stiffness. As a result, these changes affect the dynamic characteristics of the system, including the frequency-response function. Figure 13 illustrates the effect of GPL concentration on the nonlinear frequency-response of the hyperelastic nanocomposite plate. As the GPL content increases, two distinct phenomena are observed: a reduction in the maximum vibration amplitude and a progressive shift from softening-type to hardening-type behavior.

The reduction in vibration amplitude with increasing GPL concentration can be attributed to two complementary mechanisms. First, the incorporation of GPLs enhances the effective stiffness of the polymer matrix by restricting molecular chain mobility and increasing the cross-link density, which elevates the strain energy required for a given deformation. Second, the large specific surface area of GPLs may promote interfacial friction and additional energy-dissipation mechanisms at the polymer–nanoparticle interfaces. However, in the present vibration model, damping is represented by a constant linear viscous modal coefficient and is not independently calibrated as a GPL-content-dependent material property. Together, these mechanisms lead to greater energy absorption within the structure and consequently lower dynamic deformations under external excitation.

The transition from softening to hardening behavior with increasing GPL content arises from the competition between material nonlinearity and geometric nonlinearity. In pure epoxy (0 wt.% GPLs), the frequency-response curve exhibits a softening-type behavior, which is characteristic of the Mooney–Rivlin hyperelastic model employed. This softening originates from the contribution of the second invariant I_2 to the strain-energy density, which can reduce the effective stiffness under deformation patterns involving significant shear—particularly near the clamped boundaries. As GPLs are introduced and their concentration increases, the enhanced stiffness amplifies the membrane stretching effects (geometric nonlinearity) at larger amplitudes. At low to moderate GPL contents (0.2–0.4 wt.%), the material nonlinearity still dominates, and the response remains predominantly softening. However, at higher concentrations (0.6–1.0 wt.%), the geometric hardening effect becomes sufficiently strong to overcome the material-induced softening, resulting in a net hardening behavior.

The emergence of more pronounced jump phenomena and multi-stability regions at higher GPL concentrations reflects the increased complexity of the nonlinear dynamic interactions. These phenomena indicate that the system's response becomes more sensitive to initial conditions and excitation

parameters as the stiffness and energy dissipation characteristics are altered by the nanoparticles. From a design perspective, this sensitivity can be exploited to tailor the vibration isolation and energy absorption properties of the structure. The shift toward hardening behavior at higher GPL contents implies that the structure becomes more resistant to large-amplitude vibrations, which is advantageous for applications requiring dimensional stability and fatigue resistance under dynamic loads.

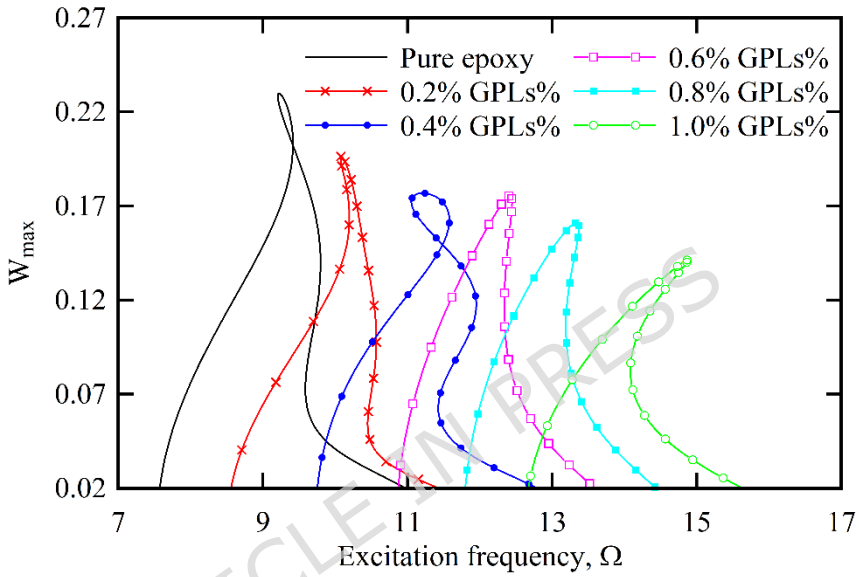

Figure 13: Effect of GPL concentration on the nonlinear frequency-amplitude response curve of the hyperelastic nanocomposite plate.

The transition from softening to hardening behavior with increasing GPL concentration is directly linked to the evolution of the Mooney–Rivlin constants C_1 and C_2 (Table 1). Physically, C_1 governs the initial shear modulus and small-strain stiffness; its increase with GPL content reflects matrix stiffening due to restricted polymer chain mobility, which amplifies geometric nonlinearity (membrane stretching) at larger amplitudes and promotes hardening. In contrast, C_2 weights the second invariant I_2, which captures shear-dominated deformations. In pure epoxy, the relatively large C_2 contribution reduces effective stiffness under shear, particularly near clamped boundaries, producing the observed softening response.

As GPL content increases, both constants rise, but their absolute magnitudes—rather than their ratio—dictate the net nonlinear behavior. From 0 to 1.0 wt.% GPLs, C_1 increases by 146% and C_2 by 150%. Despite proportional growth, the two constants govern different deformation regimes: at low amplitudes, bending-induced shear near boundaries makes C_2-driven softening dominant; at higher amplitudes, membrane stretching activates C_1-driven hardening. With enhanced C_1 at higher GPL concentrations, the hardening mechanism prevails at lower amplitudes, shifting the response from softening to hardening. Thus, the gradual transition in Figure 13 reflects the increasing predominance of C_1-induced geometric stiffening over C_2-induced material softening as GPL content rises. A concise summary of the physical mechanisms governing the transition from softening to hardening behavior with increasing GPL concentration is provided in Table 3.

Table 3: Physical interpretation of the softening-to-hardening transition with GPL concentration.

GPL Content (wt.%)	C_1 Effect (Geometric Hardening)	C_2 Effect (Material Softening)	Net Nonlinear Behavior
0 (pure epoxy)	Low (C_1=3.51 GPa)	Significant relative to C_2; I_2-induced softening near boundaries	Softening (material nonlinearity dominates)
0.2–0.4	Moderate increase	Still appreciable	Transitional (softening persists)
0.6–1.0	Large increase (up to 8.65 GPa at 1.0 wt.%)	Increased but outweighed by C_1	Hardening (geometric nonlinearity dominates)

Table 4 shows the effect of GPL concentration on the resonant frequency and maximum vibration amplitude for $F_0 = 0.3$. The results presented in Table 4 show that, within the investigated range, the resonant frequency increases monotonically with GPL concentration, reaching its maximum value at 1.0 wt.% GPLs; however, this vibration-performance improvement should be

interpreted together with the reduction in tensile strength and fracture strain observed beyond 0.8 wt.% GPLs. This increase in frequency is due to an increase in the equivalent stiffness of the system resulting from the presence of graphene nanoparticles and improved effective Young's modulus of the nanocomposite, which increases the flexural stiffness and consequently increases the natural frequency. In addition, as the GPL content increases, the maximum vibration amplitude decreases, and at the highest value (1.0 wt.% GPLs) this decrease reaches 50%. This trend indicates that GPL reinforcement can reduce the dynamic deformation of the system by increasing the effective stiffness and modifying the energy-storage characteristics of the nanocomposite. At low GPL concentrations (e.g., 0.2 wt.%), the nonlinear behavior of the system is still noticeable, but with further increases in nanoparticles, the system hardening is intensified and the frequency-response curve shifts to higher frequencies. Although the 1.0 wt.% GPL plate exhibits the highest resonant frequency and the lowest vibration amplitude in the present vibration analysis, the tensile results indicate that this concentration is beyond the mechanical-strength optimum. Therefore, the design of GPL-reinforced polymer plates should consider a trade-off between stiffness-controlled vibration improvement and agglomeration-induced reductions in strength, fracture strain, and structural reliability.

In vibration analysis, the natural frequency is more dependent on the stiffness and density of the structure than on the yield strength. Even if increasing GPLs reduces the yield strength, the frequency will still increase if its effect on increasing the Young modulus and effective stiffness is greater. This is quite noticeable for the nanocomposite sample containing 1 wt.% GPLs. Therefore, the key factor in increasing the natural frequency is the increase in flexural stiffness and effective Young's modulus due to the presence of graphene nanoparticles, which can affect the vibration behavior, even if a decrease in yield strength is observed.

It should be emphasized that the optimum GPL content depends on the design criterion considered. The value of approximately 0.8 wt.% represents

the optimum concentration for tensile strength, as the ultimate tensile strength increases up to this concentration and then decreases at 1.0 wt.% GPLs. This reduction is associated with the onset of GPL agglomeration, which creates local stress concentration zones and reduces the reinforcing efficiency of the nanoplatelets. Therefore, increasing the GPL content beyond 0.8 wt.% can reduce mechanical strength and fracture strain, even though the effective stiffness of the nanocomposite may continue to increase. From a structural reliability viewpoint, this implies a higher susceptibility to premature crack initiation, brittle fracture, and spatial variability in the material response. In contrast, the vibration response within the present range continues to benefit from the increased stiffness: the resonant frequency increases from Ω=13.8 at 0.8 wt.% GPLs to Ω=15.0 at 1.0 wt.% GPLs, while the maximum vibration amplitude decreases from $W_{\max}$=0.12 to $W_{\max}$=0.11. Hence, the 1.0 wt.% GPL plate provides improved stiffness-controlled vibration characteristics, but at the cost of reduced tensile reliability. This result indicates that the selection of GPL concentration should be based on a trade-off between mechanical strength, reliability, and vibration-performance requirements rather than on stiffness enhancement alone.

Table 4: Effect of GPL concentration on resonant frequency and maximum vibration amplitude for F_0 = 0.3

GPLs Content (wt.%)	Resonance frequency (Ω)	Frequency increase (%)	Maximum vibration amplitude (W_{max})	Amplitude reduction (%)
Pure Epoxy (0.0)	9.5	-	0.22	-
0.2	10.5	10.50%	0.19	13.60%
0.4	11.4	21.10%	0.16	27.30%
0.6	12.7	33.70%	0.14	36.40%
0.8	13.8	45.30%	0.12	45.50%
1	15	57.90%	0.11	50.00%

Figure 14(a) shows the time-domain response of the hyperelastic nanocomposite plate with 0.4 wt.% GPLs. This response shows the time evolution of the system oscillations under the applied excitation. The amplitude of the oscillations and its trend indicate the nonlinear behavior and the effect of stiffness due to the presence of nanoparticles on the dynamic response of the plate. In Figure 14(b), the phase-plane trajectory (red line) and the Poincaré map (blue dots) are presented. The phase-plane trajectory shows the overall behavior of the system in the phase space (displacement-velocity) and can identify the characteristics of periodic, chaotic, or quasi-periodic motion. The presence of discrete points in the Poincaré map indicates stable periodic behavior, while a wide distribution of points in this map may indicate chaotic behavior. In this case, observing the blue dots in a specific pattern indicates that the system's response is likely in a periodic cycle and exhibits a more regular behavior. These results confirm that GPL reinforcement modifies the stiffness and vibration characteristics of the plate and affects the response pattern in both the time and phase domains.

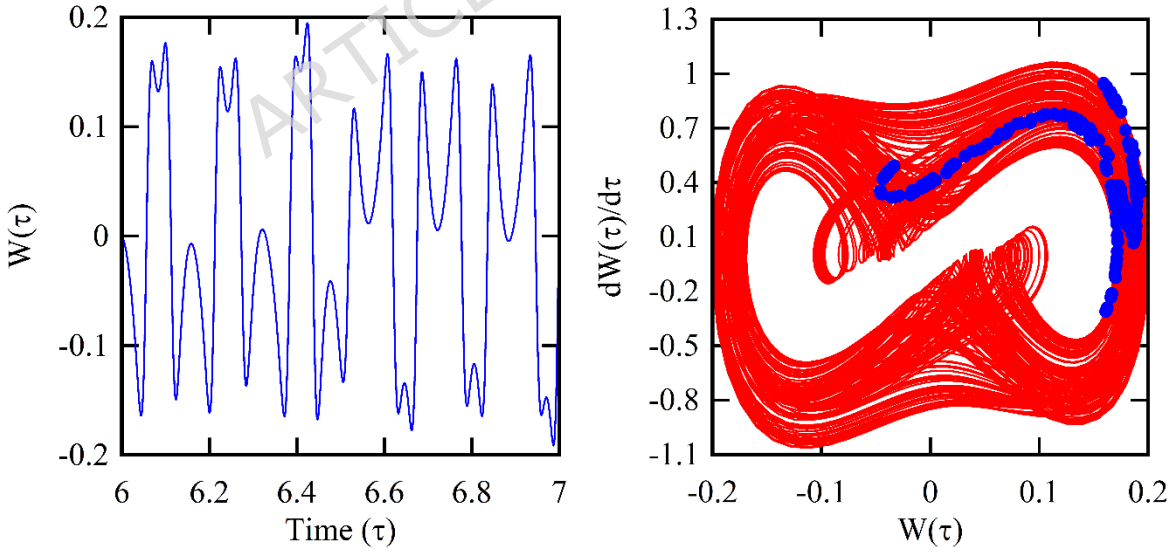

(a) (b)

Figure 14: (a) Time-domain response and (b) phase-plane trajectory (red line) and Poincaré map (blue dots) of the hyperelastic nanocomposite plate reinforced with 0.4 wt.% GPLs.

5. Limitations of the Study

Although the present study provides an experimentally calibrated nonlinear vibration framework for GPL-reinforced hyperelastic polymer plates, its scope is subject to several limitations. First, the analysis is limited to fully clamped rectangular plates modeled using the Kirchhoff–Love plate theory. Therefore, transverse shear deformation effects, which may become important for moderately thick plates, were not considered. Second, the material response was represented by an incompressible Mooney–Rivlin hyperelastic model calibrated from uniaxial tensile tests. Although this model provided good agreement with the measured tensile response, additional experimental loading modes, such as biaxial tension, planar shear, cyclic loading, and dynamic mechanical testing, could further improve the calibration and validation of the constitutive law. Third, the GPL-reinforced polymer was modeled using effective material properties, and spatially nonuniform GPL dispersion, local agglomeration, and orientation-dependent nanoplatelet effects were not explicitly introduced into the plate model. The influence of agglomeration was considered only indirectly through the experimentally measured mechanical properties. Fourth, the GPL concentration was limited to the experimentally investigated range of 0–1.0 wt.%, and the results should not be extrapolated to higher filler contents without additional experimental verification. Fifth, the concentrated mass and harmonic point force were applied at prescribed locations, and the effects of varying the mass position, force position, plate aspect ratio, and boundary condition were not systematically examined. Finally, environmental effects, temperature, humidity, fatigue, long-term viscoelasticity, and direct experimental validation of the vibration response were outside the scope of the present work. In addition, the damping term was modeled as a constant

linear viscous modal damping coefficient; possible variations of damping with GPL concentration, excitation frequency, vibration amplitude, temperature, or viscoelastic material behavior were not considered.

6. Future Work

The present study can be extended in several directions. First, future studies may examine other boundary conditions, such as simply supported, free, and mixed edge constraints, to determine how edge flexibility affects mode shapes, modal participation, resonance frequencies, nonlinear stiffness coefficients, and softening-to-hardening transitions. Second, the effects of varying the locations of the concentrated mass and harmonic point force should be investigated, because these parameters can alter modal excitation and nonlinear response branches. Third, direct experimental vibration tests on GPL-reinforced polymer plates would be valuable for validating the predicted resonance shifts, amplitude reduction, jump phenomena, phase-plane trajectories, and Poincaré maps. Fourth, the damping model can be improved by experimentally identifying damping coefficients and by considering possible dependence on GPL concentration, excitation frequency, vibration amplitude, temperature, and viscoelastic material behavior. Fifth, the present hyperelastic formulation may be extended to include visco-hyperelasticity, thermal and humidity effects, fatigue, aging, and long-term service conditions. Sixth, microstructure-informed or multiscale models could be developed to explicitly account for GPL dispersion, orientation, and agglomeration instead of representing these effects only through effective material constants. Finally, the experimentally calibrated framework may be coupled with optimization and uncertainty-quantification methods to select GPL concentration, plate geometry, and loading conditions for balanced mechanical strength, structural reliability, and nonlinear vibration-control performance.

In addition, vibration-based intelligent diagnosis and prognosis studies on elevator door systems, hemispherical resonators with mass defects, and

bearing remaining-useful-life prediction show that accurate extraction of vibration features is increasingly important for reliability assessment and health monitoring of dynamically loaded mechanical systems [64-66].

7. Conclusion

The forced vibrations of GPL-reinforced nanocomposite plates were examined in this work. The Mooney–Rivlin hyperelastic model, von Kármán geometric nonlinearity, Kirchhoff–Love plate theory, and Hamilton's principle were used to derive the coupled equations of motion. The Galerkin method and numerical solution procedures were used to solve the coupled in-plane and transverse motion equations. To obtain the hyperelastic properties of the nanocomposite plate, dumbbell-shaped tensile specimens were fabricated according to ASTM D638, and tensile tests were performed for different GPL concentrations. The measured stress–strain curves were then used to identify the Mooney–Rivlin material constants through curve fitting. The results obtained from the analyses can be summarized as follows:

1. **Effect of hyperelastic modeling:** Within the investigated loading and plate-configuration conditions, the comparison between elastic and hyperelastic formulations showed that the hyperelastic model predicts a lower oscillation amplitude and a different nonlinear hardening tendency than the equivalent linear elastic model. This difference arises from the strain-dependent stress–strain response captured by the Mooney–Rivlin formulation.
2. **Effect of concentrated mass:** For the considered central mass location and selected mass values, increasing the concentrated mass shifted the resonance response toward lower frequencies and made the hardening tendency more pronounced. The oscillation amplitude also increased in the presence of the concentrated mass, indicating the sensitivity of the dynamic response to added inertia under the studied configuration.

3. **Effect of graphene nanoplatelet concentration:** The resonant frequency increases monotonically with GPL concentration throughout the range studied, reaching its maximum value at 1.0 wt.% GPLs, where the frequency is 57.9% higher than that of pure epoxy and the maximum vibration amplitude is reduced by 50%. However, the tensile results show that 0.8 wt.% GPLs is the optimum concentration for ultimate tensile strength, while 1.0 wt.% GPLs leads to reduced strength and fracture strain due to agglomeration. Therefore, GPL content should be selected by balancing vibration-performance improvement against strength degradation and structural reliability requirements.
4. **Nonlinear dynamic analysis:** Examination of the time response, phase-plane trajectories, and Poincaré map showed that increasing the GPL content leads to a change in the oscillation pattern of the system and enhances its nonlinear behavior. These results show that GPL-reinforced plates exhibit more complex dynamic behavior than pure epoxy plates.

Overall, within the investigated material range, boundary condition, loading configuration, and modelling assumptions, the results indicate that GPL reinforcement and hyperelastic material modelling can substantially influence the predicted vibration characteristics of polymer nanocomposite plates. The proposed experimentally calibrated framework may therefore support the design of lightweight GPL-reinforced polymer plates with tailored nonlinear vibration characteristics, provided that strength, reliability, dispersion quality, and service-condition effects are also considered.

Funding Statement

This research received no specific grant from any funding agency in the public, commercial, or not-for-profit sectors.

Conflict of Interest

The authors declare that they have no conflict of interest.

Data Availability Statement

Data supporting this study are included within the article.

References

1. Hussein, A.M., L.H. Saleh, M. Diab, E. Muniyandy, A. Abdullaev, M. Latipova, B. Madaminov, S.K. Issa, M.A. Hasan, and S. Islam, (2025) Synthesis and application of tannic acid–gelatin hydrogel polymers capped silver nanoparticles as efficient and reusable nanocatalyst for A3 coupling reactions. *Journal of Organometallic Chemistry*, 1039:123766.
2. Owida, H.A., J.I. Al-Nabulsi, N.M. Turab, M. Al-Ayyad, R. Alazaidah, and N. Alshdaifat, (2025) Progression of polymeric nanostructured fibres for pharmaceutical applications. *Bulletin of Electrical Engineering and Informatics*, 14(1):409-420.
3. Hoseinzadeh, M., R. Pilafkan, and V.A. Maleki, (2023) Size-dependent linear and nonlinear vibration of functionally graded CNT reinforced imperfect microplates submerged in fluid medium. *Ocean Engineering*, 268:113257.
4. Long, X., R. Dong, J. Li, Y. Su, C. Chang, F. Jia, and X. Wan, (2025) Reverse analysis of film/substrate cohesion by indentation: A mesoscopic perspective. *International Journal of Solids and Structures*, 312:113285.
5. Long, X., Y. Li, Z. Shen, Y. Su, T. Gu, and K.S. Siow, (2024) Review of uniqueness challenge in inverse analysis of nanoindentation. *Journal of Manufacturing Processes*, 131:1897-1916.
6. Zheng, Y. and W. Niu, (2026) Coupled effects of water content and polyvinyl alcohol modification on the microstructure and mechanical behavior of montmorillonite. *Colloids and Surfaces A: Physicochemical and Engineering Aspects*:140724.
7. Rodrigue, H. and J. Kim, (2024) Soft actuators in surgical robotics: a state-of-the-art review. *Intelligent Service Robotics*, 17(1):3-17.
8. Menciassi, A. and V. Iacovacci, (2020) Implantable biorobotic organs. *APL bioengineering*, 4(4).
9. Cai, Y. and G.-L. She, (2025) Nonlinear dynamic response of rotating magneto-electro-elastic cylindrical shells under low-velocity impact. *Mechanics Based Design of Structures and Machines*:1-19.
10. Cai, Y. and G.-L. She, (2025) Nonlinear dynamic response of magneto-electro-elastic cylindrical shells subjected to moving load. *Mechanics of Advanced Materials and Structures*:1-12.
11. Zheng, F., W. Zhang, X. Yuan, and Y. Zhang, (2023) Radial nonlinear vibrations of thin-walled hyperelastic cylindrical shell composed of Mooney–Rivlin materials under radial harmonic excitation. *Nonlinear Dynamics*, 111(21):19791-19815.
12. Zhang, J., W. Zhang, and Y. Zhang, (2024) Nonlinear vibrations of porous-hyperelastic cylindrical shell under harmonic force using harmonic balance and pseudo-arc length continuation methods. *Thin-Walled Structures*, 198:111767.
13. Xie, F., Y. Qu, Y. Li, and G. Meng, (2024) Nonlinear acoustic radiation induced by in-plane vibration of hyperelastic rubber-like plates subject to dynamic loads. *Wave Motion*, 127:103277.
14. Foroutan, K., H. Ahmadi, and S. Karimi, (2024) Nonlinear vibration and resonance analysis of a rectangular hyperelastic membrane surrounded by nonlinear elastic foundation. *Mechanics Based Design of Structures and Machines*, 52(7):4616-4641.

15. Cui, W., L. Zhao, Y. Ge, and K. Xu, (2024) A generalized van der Pol nonlinear model of vortex-induced vibrations of bridge decks with multistability. *Nonlinear Dynamics*, 112(1):259-272.
16. Zhai, Y., X. Tian, C. Gao, C. Li, S. Liang, X. Yu, and C. Wang, (2026) Study on the Vibration and Damping Behavior of Composite Cylindrical Shells with Embedded Varying Amounts of Damping Layers. *Journal of Vibration Engineering & Technologies*, 14(3):136.
17. Zhang, P., N. Li, H. Tian, J. Li, and H. Arvin, (2026) Characterization of bistable frequency responses in nonlinear oscillations of flow-filled graphene-reinforced pipes under various resonances. *Engineering Structures*, 353:122250.
18. Shitikova, M. and V. Kandu. *Force driven nonlinear vibrations of a thin plate with 1: 1 internal resonance in a fractional viscoelastic medium*. in *IOP Conference Series: Materials Science and Engineering*. 2019. IOP Publishing.
19. Karimi, S., H. Ahmadi, and K. Foroutan, (2023) Nonlinear vibration and resonance analysis of a rectangular hyperelastic membrane resting on a Winkler–Pasternak elastic medium under hydrostatic pressure. *Journal of Vibration and Control*, 29(5-6):1323-1341.
20. Hosseini, S., G.H. Rahimi, and Y. Anani, (2021) Nonlinear analysis of hyperelastic plates using first-order shear deformation plate theory and a meshless method. *Amirkabir Journal of Mechanical Engineering*, 53(4):2331-2346.
21. Parhi, J.D., T. Roy, and S.K. Panda, (2025) Nonlinear dynamic and energy absorption characteristics of auxetic graded nanotube-reinforced polymeric composite beams. *International Journal of Structural Stability and Dynamics*.
22. Parhi, J.D., T. Roy, A. Kumar, and S.S. Patnaik, (2024) Nonlinear dynamic study of FG-GFRC-NPR structures. *Engineering Research Express*, 6(3):035537.
23. Parhi, J.D. and T. Roy, (2025) Nonlinear vibration and energy absorption responses of auxetic sandwich nanocomposite structures. *Journal of Vibration Engineering & Technologies*, 13:164.
24. Parhi, J.D. and T. Roy, (2023) Chaotic vibration analysis of auxetic nanocomposite structures. *Journal of Vibration and Control*, 29(19-20):4687-4705.
25. Liang, J., Z. Li, F. Ye, Y. Cao, Y. An, X. Fan, and Q. Song, (2026) Graphene-Skinned Fiber with Fine-Tunable Electrical Resistance via Radical and Substrate Engineering for Electromagnetic-Thermal Fabric. *Nano-Micro Letters*, 18(1):263.
26. Islam, M. and R. Sarker, (2025) Identification of Nanoparticle Agglomeration in Polymer Plates Reinforced with Carbon Nanotubes by Use of Active Thermography and Deep Learning-Based Image Processing. *Advances in Engineering and Intelligence Systems*, 004(02):121-129.
27. Liu, Y., J. Li, Z. Chen, X. Niu, Z. Liu, Z. Wang, and D. He, (2026) Effect of annealing temperature on microstructure and properties of stainless steel/copper composite strips. *Advanced Composites and Hybrid Materials*, 9(2):103.
28. Xiao, C., J. Peng, Y. Jiao, Q. Shen, Y. Zhao, F. Zhao, and Q. Song, (2024) Strong and Tough Multilayer Heterogeneous Pyrocarbon Based Composites. *Advanced Functional Materials*, 34(51):2409881.
29. Fazeli, Y., Z. Nourbakhsh, S. Yalameha, and D. Vashaee, (2025) Anisotropic elasticity, spin–orbit coupling, and topological properties of ZrTe2 and NiTe2:

a comparative study for spintronic and nanoscale applications. *Nanomaterials*, 15(2):148.
30. Yang, Z., H. Wu, S. Zhao, J. Yang, A. Liu, J. Lv, and J. Fu, (2023) Nonlinear static bending and dynamic behaviors of graphene platelets reinforced dielectric porous arches. *Aerospace Science and Technology*, 143:108729.
31. Shadhar, M.H., M.H. Abdullah, Z.A. Mohammed, V. Jain, N. Shari, R. Kumar, I. Mahariq, M.R. Al Asiri, and S. Islam, (2025) Effect of Rotational Loads and Various Characteristics of Graphene Nanoplatelets on the Free Vibration Results of Nanocomposite Shell. *Journal of Vibration Engineering & Technologies*, 13(1):124.
32. Tian, H., (2023) Size-Dependent Dynamic Behavior of Axially Moving Graphene Nanosheets Using Nonlocal First-Order Shear Deformation Theory. *Advances in Engineering and Intelligence Systems*, 002(02):41-50.
33. Guo, H., Y. Li, B. Zhao, Y. Guo, Z. Xie, X. Lu, and A. Morina, (2026) Study on transient lubrication of floating bush in high-pressure fuel pump coupling with camshaft bending vibration. *Tribology International*, 215:111357.
34. Liang, D., H. Hu, and Y. Wu, (2025) Geometric design and dynamic characteristics analysis of a novel herringbone planetary gear. *Proceedings of the Institution of Mechanical Engineers, Part K: Journal of Multi-body Dynamics*, 239(3):234-253.
35. Liu, Q., Q. Liu, Y. Zhou, J. Liu, Y. Dai, S. Chen, and T. Lai, (2025) Identifying vibration characteristics of hemispherical resonators with mass defects. *International Journal of Mechanical Sciences*, 306:110856.
36. Yang, Z., S.-K. Lai, Z. Chen, J. Yang, A. Liu, and J. Fu, (2025) Dynamic analysis of electrically prestressed highly aligned graphene-reinforced dielectric porous arches under large deformation. *Communications in Nonlinear Science and Numerical Simulation*, 147:108876.
37. Fan, Y.-H. and G.-L. She, (2025) Nonlinear transient response of graphene platelets reinforced metal foams beam considering initial geometrical imperfection and viscoelastic elastic foundation. *Computers and Concrete*, 35(1):59.
38. Fan, Y.-H., G.-L. She, and M.A. Eltaher, (2025) Nonlinear vibrations of two-directional functionally graded spinning annular plates with variable thickness. *Thin-Walled Structures*, 216:113627.
39. Fan, Y.-H., G.-L. She, and C. Li, (2025) Nonlinear transient response analysis of revolution doubly curved shells. *Archives of Civil and Mechanical Engineering*, 25(3):145.
40. Bai, B., H. Li, X. Yi, J. Tang, Y. Liu, F. Zhang, and X. Li, (2026) A three-level discretization framework for dynamic behaviors of graphene-coated rotational blades with preset-angle sandwich structure under complex loads. *Scientific Reports*.
41. Gai, J., X. Yang, and Y. Zhao, (2026) Electroacoustic wave scattering from cylindrical inhomogeneities in transversely isotropic piezoelectric composites. *Materials & Design*, 261:115296.
42. Kang, H., Z. Li, T. Liu, W. Yuan, and J. Jing, (2024) Free vibration analysis of pre-twisted rotating dovetailed blade under the flexible connection with macro-micro rough contact topography. *Thin-Walled Structures*, 201:112039.
43. Zhang, Z., Y. Wang, and W. Zhang, (2023) Temperature- and moisture-dependent aeroelastic stability of graphene platelet reinforced nanocomposite

lattice sandwich plates subjected to supersonic flow. *Aerospace Science and Technology*, 138:108348.
44. Wang, Y., Z. Zhang, and W. Zhang, (2024) Suppression of nonlinear aeroelastic responses of graphene platelet-reinforced composite lattice sandwich plates using a nonlinear energy sink. *Nonlinear Dynamics*, 112(15):12925-12939.
45. Wang, Y. and W. Zhang, (2022) On the thermal buckling and postbuckling responses of temperature-dependent graphene platelets reinforced porous nanocomposite beams. *Composite Structures*, 296:115880.
46. Ma, Z.-S., G.-L. She, and C. Li, (2025) Nonlinear thermal flutter analysis of graphene platelets reinforced metal foam arbitrary quadrilateral plates. *Archives of Civil and Mechanical Engineering*, 25(4):203.
47. She, G.-L., Z.-S. Ma, C. Li, and M. Eltaher, (2025) Geometrically nonlinear transient response of graphene platelets reinforced metal foams arbitrary quadrilateral plates under blast load. *Thin-Walled Structures*, 210:113018.
48. Cheng, Y.-H., G.-L. She, and M. Eltaher, (2025) Nonlinear internal resonance of graphene-reinforced metal foam plates with initial geometric imperfection under non-uniform temperature field. *Aerospace Science and Technology*, 165:110491.
49. Cheng, Y.-H. and G.-L. She, (2025) Nonlinear transient response of rotating graphene reinforced metal foam beams with cracks. *International Journal of Structural Stability and Dynamics*.
50. Wang, X., J. Han, H. Xu, H. Ji, Z. Yue, R. Zhang, B. Li, Y. Ji, Z. Li, and P. Wang, (2024) Nonlinear mechanical behaviour and visco-hyperelastic constitutive description of isotropic-genesis, polydomain liquid crystal elastomers at high strain rates. *Journal of the Mechanics and Physics of Solids*, 193:105882.
51. Khaniki, H.B., M.H. Ghayesh, R. Chin, and M. Amabili, (2022) A review on the nonlinear dynamics of hyperelastic structures. *Nonlinear Dynamics*, 110(2):963-994.
52. Basar, Y. and D. Weichert, *Nonlinear continuum mechanics of solids: fundamental mathematical and physical concepts*. 2013: Springer Science & Business Media.
53. Amabili, M., (2016) Nonlinear vibrations of viscoelastic rectangular plates. *Journal of Sound and Vibration*, 362:142-156.
54. Xiao, X., C. Xiao, and Y. Yin, (2022) A hyperelastic model for corneal stroma accounting for cross-linking and damage. *International Journal of Engineering Science*, 176:103701.
55. Chen, W. and Y.-P. Zhao, (2022) Thermo-mechanically coupled constitutive equations for soft elastomers with arbitrary initial states. *International Journal of Engineering Science*, 178:103730.
56. Rezaee, M. and V.A. Maleki, (2024) On the complex mode shapes and natural frequencies of clamped-clamped fluid-conveying pipe. *Applied Ocean Research*, 150:104113.
57. Farzad, R. and V. Lotfi, (2023) Modal analysis of concrete arch dam–reservoir–massed foundation system in frequency domain. *Proceedings of the institution of civil engineers-structures and buildings*, 176(4):244-256.
58. Pourreza, T., A. Alijani, V. A. Maleki, and A. Kazemi, (2025) Nonlinear vibrations of graphene nanoplates with arbitrarily orientated crack located in magnetic field using nonlocal elasticity theory. *International Journal of Structural Integrity*, ahead-of-print(ahead-of-print).

59. Rezaee, M., R. Fathi, and V.A. Maleki, (2025) Dynamic analysis and uncertainty modeling of viscoelastic beam response to fluid stimulation: Insights into nonlinear effects and velocity uncertainties. *Applied Ocean Research*, 157:104487.
60. Farzad, R. and P. Brewick, (2025) Selecting and identifying hysteretic models for steel damper pairs using Full-Scale testing data. *Journal of Engineering Mechanics*, 151(10):04025054.
61. Brewick, P.T. and R. Farzad, (2025) Hierarchical bayesian calibration of Bouc–Wen hysteretic models with applications to seismic isolators. *Mechanical Systems and Signal Processing*, 237:113021.
62. Allgower, E.L. and K. Georg, *Numerical continuation methods: an introduction*. Vol. 13. 2012: Springer Science & Business Media.
63. Breslavsky, I.D., M. Amabili, and M. Legrand, (2014) Nonlinear vibrations of thin hyperelastic plates. *Journal of Sound and Vibration*, 333(19):4668-4681.
64. Guo, R., J. Yi, and X. Luo, (2025) An efficient classification and error correction knowledge distillation framework for remaining useful life prediction of bearings in air turbine starter. *Neurocomputing*, 657:131611.
65. Kang, H., Z. Li, T. Liu, H. Han, X. Liu, Q. Hu, and G. Zhang, (2025) An analytical modeling for free vibration of pre-twisted mechanical metamaterial sandwich blade with cube-centered truss lattice core. *Engineering Structures*, 343:121257.
66. Wan, A., X. Tong, K. AL-Bukhaiti, Z. Zhou, Y. Su, and X. Cheng, (2025) Intelligent fault diagnosis for elevator door systems using variational mode decomposition and multi-scale convolutional networks. *Journal of the Brazilian Society of Mechanical Sciences and Engineering*, 47(10):508.